Perilipin 4 repetitive region forms amyloid fibrils promoted by a genetic expansion found in myopathy patients

Charbel Choufani[1‡], Nicolas Fuggetta[1‡], Bayane Sabbagh[1], Cyril Moulin[1], Céline Franckhauser[1], Sebastien Lyonnais[2], Tinkara Perme[1], Ana-Andreea Arteni[3], Sophie Pagnotta[4], Sylvie Rouquier[1], Alessandra Ruggieri[5], Luc Bousset[3*], Alenka Čopič[1**]

[1] Montpellier Cell Biology Research Center - CRBM, University of Montpellier, CNRS, Montpellier, France
[2] CEMIPAI, University of Montpellier, UAR 3725 CNRS, Montpellier, France.
[3] Université Paris-Saclay, CEA, CNRS, Institute for Integrative Biology of the Cell (I2BC), Cryo-electron Microscopy Facility, CRYOEM-Gif, Gif-sur-Yvette, France.
[4] Microscopy center (CCMA), Valrose, Université Côte d'Azur (UniCA), Nice, France.
[5] Neuroimmunology and Neuromuscular Diseases Unit, Fondazione IRCCS Istituto Neurologico Carlo Besta, 20133 Milan, Italy.
[6] Laboratory of Neurodegenerative Diseases, Institut François Jacob, MIRCen, CEA, CNRS, Fontenay-aux-Roses, France.

‡These authors contributed equally to this work.

*Correspondence: luc.bousset@cnrs.fr
**Correspondence (Lead contact): alenka.copic@crbm.cnrs.fr

Summary

Perilipin 4 (PLIN4) belongs to the family of perilipins – proteins that localize to lipid droplets (LDs). PLIN4 contains a giant (≈ 1000 aa) amphipathic helix, which folds on the LD surface and can substitute for phospholipids, thereby regulating LD surface tension. This region of PLIN4 is arranged in tandem repeats of 33 aa. Genetic expansion of this region is associated with skeletal muscle dysfunction in patients suffering from a late-onset vacuolar myopathy (MRUPAV). We demonstrate that purified fragments of the PLIN4 repetitive region form amyloid fibrils as characterized by cryo-EM and atomic force microscopy. The MRUPAV mutation drastically increases the kinetics of fibril formation and induces aggregation in budding yeast. The propensity to aggregate depends on the number of identical repeats and their sequence, and is strongly attenuated by the presence of lipid droplets, suggesting putative intervention strategies and an explanation for the observed tissue bias of the disease.

Key words:

Perilipin, lipid droplet, amyloid, genetic expansion, coding repeats, degenerative disease, myopathy, skeletal muscle

Introduction

Many degenerative diseases are associated with protein aggregation [1]. Protein aggregates can be amorphous or forming an ordered phase, with the most highly ordered aggregates presenting as amyloid fibrils, where protein units are stacked within a highly stable cross-β fold. Some well-known examples of amyloid forming proteins include α-synuclein, Aβ protein, tau and huntingtin protein [2]. Amyloid fibrils represent an alternative conformation, which can be adopted by the wild-type protein and may be promoted by genetic mutations. For example, wild-type α-synuclein is found accumulated in the dense clusters termed Lewy bodies in the brains of patients for which Parkinson's disease is associated with ageing. However, early-onset familial form of the disease is linked to genetic mutations in α-synuclein that can promote its aggregation *in vitro* [3]. Atomic structures of amyloid fibrils have been determined and show how amino-acid residues are stacked in the cross-β fold [4–6]. Only specific segments of amyloid forming proteins are engaged in the amyloid core, ranging from 15 to 199 amino acids (aa), representing 5 to 100% of the total protein sequence length [7,8].

Many amyloid-forming protein regions are repetitive in nature, and repetitive sequences are more likely to form amyloids [9]. For example, the amyloid-forming region (AR) of α-synuclein contains imperfect 11-aa repeats [10,11]. Another well-known example is tau protein, whose AR is comprised of 4 microtubule-binding repeats [12]. Splicing produces 3 or 4 repeat variants that have different aggregation propensities [13]. In the case of huntingtin protein, its AR is comprised of poly-Q repeats [14,15]. Genetic mutations that result in the expansion of the poly-Q region lead to huntingtin disease, and the severity of the disease is linked to the length of the poly-Q expansion.

A rare progressive distal myopathy that leads to loss of skeletal muscle was first described in 2004 in a large multi-generation family [16] and was termed MRUPAV, for "myopathy with rimmed ubiquitin-positive autophagic vacuolation" (MIM #601846). Distal myopathies are genetically-diverse diseases, often characterized by the presence of protein aggregates in muscle fibers or defects in protein folding or aggregate clearance pathways [17]**.** A. Ruggieri and colleagues have recently shown that this autosomal dominant disease is linked to a large coding expansion in *PLIN4* [18,19]. In muscle biopsies of patients carrying the *PLIN4* expansion, perilipin 4 (PLIN4) is the most abundant protein that accumulates in protein-dense enlarged vacuoles and is also observed in subsarcolemmal aggregates that are positive for ubiquitin and autophagy markers p62 and NBR1, suggesting activation of the aggrephagy pathway for aggregate clearance [20,21]. PLIN4 contains an unusually long central repetitive region, composed of about 30 highly conserved 33-aa repeats, which bear similarity to the 11-aa repeat region of α-synuclein [22,23]. The coding expansion identified in MRUPAV patients results in additional 33-aa repeats in the repetitive region [19]. The high repetitiveness of the corresponding DNA region and lack of any nucleotide change in the genetic expansion explains why this mutation was so difficult to identify. Furthermore, MRUPAV patients exhibit clinical symptoms similar to other vacuolar myopathies. Nevertheless, additional families with muscular degeneration linked to *PLIN4* expansion have recently been reported, with one family carrying an even longer expansion, linked to an earlier disease onset and more proximal muscle involvement [24,25].

PLIN4 belongs to the family of perilipins, which are the most abundant proteins on the surface of lipid droplets (LDs) – cellular organelles dedicated to the storage of energy in the form of neutral lipids [26,27]. LDs are prominent in myofibrils and provide energy for muscle contraction. Their number and properties can vary in disease states, such as type II diabetes, or with training [28,29]. PLIN4 is highly expressed in skeletal muscle and in adipocyte cells [30–32]. Whereas perilipins are generally considered as regulators of LD metabolism, the molecular function of PLIN4 remains enigmatic. Recent evidence suggests that PLIN4 is important for regulation of LD stability, in particular during increased LD production [33]. On a population level, analysis of whole-exome sequencing data from a large cohort shows that loss-of-function mutations in *PLIN4* correlate with unfavorable body fat distribution and metabolic profiles in humans [26,34]. These studies point to an important role of PLIN4 in the regulation of cellular lipid metabolism.

We have previously shown that the repetitive region of PLIN4 directly interacts with the LD surface and is required for PLIN4 targeting in cells, where PLIN4 can be found both in the cytosol and on LDs. The repetitive region is disordered in solution and it folds into an amphipathic helix in contact with the LD surface, with which it interacts in a length-dependent manner [22,35]. Amphipathic helices are common in proteins that interact with LDs. However, PLIN4 is unique in the size and highly repetitive nature of its amphipathic helix sequence. Interestingly, the much shorter and imperfectly-repetitive region of α-synuclein, which forms amyloid fibrils, has also been shown to target LDs [22,36,37]. LDs have been observed in vicinity of α-synuclein aggregates and are generally implicated in protein quality control [38–40].

Here, we explore the molecular mechanism of the *PLIN4*-linked myopathy. Using *in vitro* approaches with purified fragments of PLIN4, we show that the PLIN4 repetitive region is prone to forming amyloid fibrils, and that this propensity is drastically increased by the genetic expansion, which increases the number of identical 33-aa repeats in PLIN4. It is precisely these identical repeats that promote amyloid formation in solution, and the effect is further promoted by a decrease in the interaction with LDs. We therefore propose that the genetic expansion carried by the MRUPAV patients represents a gain-of-function mutation that promotes the aggregation of PLIN4, interfering with muscle contraction. In agreement with this hypothesis, we don't observe a significant effect of the genetic expansion on the behavior of PLIN4 repetitive region in solution or on its interaction with LDs in cells or *in vitro.* Understanding the aberrant nature of PLIN4 fibrils may open the door towards design of specific treatments for the affected patients, and also promote our understanding of the interplay between lipid metabolism and amyloid-based degenerative disorders.

Results

Fragments of PLIN4 can form fibrils in solution

Human PLIN4 (Uniprot Q96Q06) contains a long repetitive region composed of 29 x 33-aa repeats, flanked by a disordered N-terminal region and a folded C-terminal domain (Fig. 1A). The protein has a narrow expression profile, mostly restricted to highly-differentiated cells such as mature

adipocytes, skeletal muscle and breast tissue [31]. In cultured cells, it can be observed in the cytosol or on LDs; in cultured adipocytes, it is recruited to LDs after exogenous addition of fatty acids to burst LD production [33,41]. The central repetitive region of PLIN4 is required for the interaction with LDs [22,35].

We previously purified fragments of the repetitive region of PLIN4 and demonstrated that they were unfolded in solution and folded into an amphipathic helix in contact with a lipid surface [22]. This amphipathic helix can replace phospholipids on the surface of LDs and form stable lipid particles [33,35]. Unexpectedly, when we incubated purified PLIN4-20mer, comprising 20 x 33-aa repeats (Figure 1A), at room temperature for a prolonged time (> 1 week) and at a high protein concentration (1.5 mg/ml), followed by negative stain electron microscopy (EM), we could observe filaments with a regular appearance (Figure S1A). The finding of A Ruggieri and colleagues [19] that an elongated PLIN4 accumulates in the muscle tissue of patients with the MRUPAV vacuolar myopathy, possibly representing PLIN4 aggregates, prompted us to re-evaluate the formation of PLIN4 fibrils under controlled conditions.

We started by purifying a fragment of wild-type PLIN4, termed 12mer[260:], comprising the region of PLIN4 starting aa 260 (numbering Uniprot Q96Q06) and containing 12 x 33-aa repeats (396 aa). The first three repeats in this region are expanded 3 times in MRUPAV patients due to the genetically-encoded expansion (Figure 1A and S1B). We incubated the purified protein at different concentrations at 37°C under agitation in the presence of ThioflavinT (ThT), a fluorescent compound whose intrinsic fluorescence drastically increases after intercalation into protein fibrils (amyloids) [42]. We observed a large and concentration-dependent increase in ThT fluorescence over the course of several days. (Figure 1B). For comparison, we used a previously purified PLIN4-12mer fragment comprising a region of the same length downstream of 12mer[260:], now renamed PLIN4-12mer[524:] (Figure 1A) [22]. Under the same conditions, this fragment showed almost no increase in ThT fluorescence even at the highest concentration (Figure 1B). We next assessed the formation of fibrils using a pelleting assay and observed a good correlation with the ThT assay (Figure 1C): before incubation, both proteins remained in the supernatant, whereas after incubation at 37°C for 100 h, ~10% of 12mer[260:] at 0.25 mg/ml and ~50% of 12mer[260:] at 1 mg/ml were found in the pellet fraction. In contrast, 12mer[524:] at 1 mg/ml remained soluble. Analysis of protein samples after ThT incubation by negative-stain EM consistently revealed abundant and uniform fibrils formed by 12mer[260:] (Figure 1D). For 12mer[524:] we could observe fibrils in only one experiment, following a prolonged incubation at a high protein concentration (2 mg/ml, Figure S1C). Together, these results suggest that the repetitive region of wild-type PLIN4 is prone to fibril formation, in particular the region comprising the repeats that are multiplied in MRUPAV patients.

Given the different behaviors of the two 12mer fragments in our aggregation assays, we asked whether they differ in their secondary structure in solution. By circular dichroism (CD), both fragments display spectra typical for unstructured proteins, whereas they show a strong shift to α-helical spectra in the presence of 50% trifluoroethanol (TFE), as previously shown for 12mer[524:] (Figure 1F) [22]. In agreement, both fragments are highly susceptible to limited proteolysis by subtilisin, which is indicative of high exposure of peptide bonds all along the sequence, i.e., lack of tertiary structure. By contrast, both fragments become more resistant to proteolysis by the addition of liposomes, indicating their folding on the liposome surface (Figure

1G) [43]. Of note, these liposomes contain diphytanyl phospholipids with branched acyl chains that promote PLIN4-12mer binding to bilayers. We have previously shown PLIN4-12mer shows weak affinity towards standard bilayers due to its low hydrophobicity, and instead preferentially localizes to LDs in cells [22]. We conclude that the different aggregation propensities of the PLIN4 repetitive region are not due to differences in their structure in solution or their ability to fold into a α-helix.

Structural analysis reveals that PLIN4 fibrils are amyloids

To determine the characteristics of the fibrils formed by PLIN4 repetitive region, we analyzed the 12mer[260:] fibrils by cryo-EM and atomic force microscopy (AFM) in liquid (Figure 2). The cryo-EM analysis of vitrified plin4 fibrils allows extraction of 20.000 filament segments. Segments were boxed into 788x788 Å squares and aligned with Relion4 helical module (Figure 2A). Two main classes were identified, thin and thick filaments. The pattern analysis of filaments by Fourier transform unequivocally shows that PLIN4 fibrils are amyloid in nature, as revealed by the 4.77 Å amyloid spacing which is the signature of a cross-β pattern (Figure 2B and 2C) [2]. However, despite the high quality of our cryo-EM data, averaging revealed heterogeneity within the fibrils, suggesting that there might be different modes of stacking between the repeats of the 12mer[260:] PLIN4 fragment during amyloid growth. Observation of 12mer[260:] fibrils by AFM revealed typical amyloid fibrils heterogeneous in length, showing a left-handed periodic twist and a maximum height between 7 and 8 nm (Figure 2D). Periodicity analysis by AFM [44] revealed an average distribution around 60 nm, but with significant variations confirming the heterogeneity noted by CryoEM (Figure 2E-F). In addition, the height profiles show atypical variations suggesting gaps in the fibril structure (Figure 2E). Multiple scanning on single fibrils at relatively low setpoint (300 pN) eventually led to fibril disruption (Figure 2G), which started with punctual deformations of the fibril axis, followed by breaks generating destructed ends with short sections around 3-4 nm in diameter. Careful examination of the induced breaks did not showed 2 identifiable fibrils, thus suggesting the formation of a single fibril formed by PLIN4-12mer[260:].

In summary, this structural analysis shows that the repetitive region of PLIN4 can form amyloid fibrils with variable periodicity and structural heterogeneity, and raises questions regarding how the 33-aa repeats of PLIN4 interact within the amyloid fibril.

Influence of PLIN4 repeat sequence and number on fibril formation

Having determined that PLIN4 repetitive region can form amyloid fibrils *in vitro*, we wanted to understand how the exact nature and organization of the 33-aa repeats influence amyloid fibril formation. In particular, we wondered if any feature of the extended version of PLIN4, present in the muscle fibrils of MRUPAV patients, would increase the propensity of the protein towards amyloid formation.

Comparison of the sequences of the 33-aa repeats of WT PLIN4 shows a high level of identity between the repeats (Figure 3A). Overall, the repeats display unique aa composition, with some aa's being highly over-represented (valine, glycine, threonine), under-represented (arginine, glutamic acid, phenylalanine) or completely absent (tryptophan, tyrosine, histidine) [35] (Figure 3B).

Among all repeats, three consecutive repeats, r6, r7 & r8 (aa260 – 358) are identical, and this is precisely where the mutant PLIN4 repeat-expansion occurs in the MRUPAV myopathy patients, resulting in 12 identical repeats and expanding the total length of the protein by 297 aa (9 x 33 aa repeats) [19] (Figure 3A).

We first asked how the exact sequence of PLIN4 repeats influences amyloid formation. We used amyloid prediction algorithms ArchCandy2, Pasta and Tango, included in the TAPASS pipeline [45–48], to determine the size and position of amyloidogenic regions (ARs) within the PLIN4 sequence. The majority of predicted ARs were identified within the repetitive region. Their median length was 27 aa, and their position matched the definition of the reading frame of the repeats, *i.e.,* they mapped within the individual repeats (Figure S2 and Table S1), meaning that these segments could form the amyloid core of PLIN4 fibrils. We then used ArchCandy 2 to predict the propensity of individual repeats to form amyloids (Figure 3C and Table S1). The prediction is plotted as a heatmap for individual repeats and shows amyloid propensity varies between individual repeats (Figure 3C). To experimentally assess these results, we analyzed fibril formation in the ThT assay for three 33-aa synthetic peptides corresponding to three PLIN4 repeats with different amyloidogenic propensities (intermediate, high and low), 1mer[260:] (repeat r6 that is multiplied in patients), 1mer[656:] (r18) and 1mer[755:] (r21), respectively. We observed rapid fibril formation for 1mer[260:] with a very short lag phase, and the rate of fibril formation was even higher for 1mer[656:] at similar peptide concentrations. By contrast, 1mer[755:] did not show any increase in ThT signal even at the highest concentration (1 mg/ml) (Figure 3D). However, we were not able to observe any fibrils formed by 1mer[260:] or 1mer[656:] by negative stain EM or by AFM, whereas large μm-sized particles could be observed by fluorescence microscopy after aggregation in the presence of ThT (see Figure S4B). Rapid polymerization of these peptides may lead to anisotropic growth and formation of large clumps, which could even be observed by eye in the test tubes.

We also analyzed the formation of fibrils by longer fragments containing 4 repeats from different parts of the PLIN4 repetitive region, which were purified from *E. coli* (Figure S3A). Surprisingly, the fragment 4mer[260:], comprising PLIN4 region 260-523 (Figure 3A), aggregated with a similar kinetics as the single repeat 1mer[260:] at high protein concentration (0.5 mg/ml, Figure 3E). This was despite its 4-times higher length, which we would expect to slow down the aggregation kinetics due to higher flexibility of the polypeptide chain, as was the case for 12mer[260:] (Figure 3F). However, in contrast to 1mer[260:], the aggregation kinetics of 4mer[260:] was largely concentration-independent and occured even at 20x lower protein concentration (0.03 mg/ml, Figure S3B). Of note, unlike all other purified PLIN4 fragments used in these experiments, 4mer[260:] contains a T7 tag of 13 aa at its N-ter, which was introduced during cloning (see Table S2). This tag likely slightly inhibits the aggregation of this PLIN4 fragment (see the behavior of MBP-fusion constructs described in the next section. Other 4mer fragments (4mer[326:], 4mer[557:], and 4mer[689:]) aggregated with different kinetics that were more or less concentration dependent, with 4mer[557:] showing the most similar behavior to 4mer[260:], 4mer[326:] aggregating more slowly, and 4mer[689:] requiring a much higher concentration for robust aggregation (Figure S3B-E). This data is in agreement with the prediction that individual repeats have different amyloidogenic propensities and shows that combination of different repeats can lead to variable outcomes.

Identical repeats in expanded PLIN4 strongly promote fibrillation

A unique feature of the region of the PLIN4 sequence that is expanded in MRUPAV patients is that it contains 3 identical repeats (r6-r8). These three identical repeats are represented by 1mer[260:], and all three are included in PLIN4-4mer[260:] and in PLIN4-12mer[260:]. The presence of identical repeats in this region could promote amyloid formation by prioritizing intra-molecular stacking. To test this hypothesis, we expressed and purified a 12mer fragment termed 12merMUT, which contains 9 identical repeats, *i.e.*, 3-fold more than 12mer[260:] that represents the WT PLIN4 sequence (Figure 3A and S4A,B). Purified 12merMUT displayed an extremely fast aggregation kinetics, orders of magnitude faster than 12mer[260:], even at >10-fold lower protein concentration (Figure 3F and S4C). Furthermore, we could detect aggregate formation already during purification of 12merMUT (Figure S4A,B). Unlike for the 1mer peptides or 12mer[260:], aggregation kinetics of 12merMUT were similar over a range of concentrations. Furthermore, the ThT fluorescence signal displayed a high scatter, suggesting that the rapid polymerization could be leading to formation of large particles. Indeed, we could observe large (μm-sized) particles by fluorescent microscopy (Figure S4D), whereas we were not able to detect any fibrils by EM or by AFM.

To circumvent the problem of rapid aggregation and obtain fibrils comprised of identical repeats, we prepared constructs where 2, 3 or 4 copies of 1mer[260:] were fused to maltose-binding protein (MBP), followed by a tobacco etch virus (TEV) protease restriction site (Figure 3G). The MBP tag increased the solubility of the tandem 33-aa identical repeats, and the fusion proteins were purified by affinity chromatography and tested in the ThT aggregation assay at different protein concentrations in the presence or absence of TEV to cleave off the N-terminal tag. As expected, at about the same mass concentration of each MBP construct, meaning the same concentration of the 33-aa repeat in each reaction, aggregation efficiency in the presence of TEV increased with the number of identical repeats in the same construct, *i.e.*, from 2x to 4x (Figure 3G). For the longest construct, MBP-4x1mer[260:], we observed aggregation by ThT fluorescence even in the absence of TEV (Figure 3G, right panel). By negative stain EM, we could observe long fibrils in this sample (decorated with spherical buds), whereas in the +TEV sample, some shorter uniform fibrils were observed among more abundant and amorphous aggregates (Figure 3H). No fibrils could be observed with the 2x or the 3x constructs. We obtained more abundant thick fibrils (~20 nm in diameter) when MBP-4x1mer[260:] was purified using a longer induction to augment protein concentration, and treatment of these fibrils with pronase to shave off MBP reduced their thickness (5-8 nm in diameter) (Figure S5A and S5B). Analysis of the MBP-4x1mer[260:] fibrils by cryo-EM yielded a similar classification as for the 12mer[260:] fibrils, with thick and thin polymorphs (Figure S5C and S5D), suggesting that these fibrils contain a similar functional folding unit. We conclude that multiplication of identical repeats within the same peptide promotes fibril formation, which can be slowed-down by a globular tag.

Based on these results, we propose that the multiplication of identical repeats in mutant PLIN4, expressed in skeletal muscle of myopathy patients, leads to more pronounced aggregation *via* intramolecular interactions that promote in-register β stacking (Figure 3I). This model is in agreement with the large increase in aggregation kinetics when comparing two PLIN4 fragments

of the same length (12 x 33 aa = 396 aa), where one contains three times more identical repeats (Figure 3F). Furthermore, the model is supported by the observation that when we multiplied the number of identical repeats within the same peptide (from 2 to 4), the aggregation kinetics was increased even though the total number of identical repeats was kept similar between the reactions with different fragments (Figure 3G). Furthermore, we did not observe any difference in the localization of full-length wild-type or mutant PLIN4, fused to GFP, and stably transfected HeLa cells (Figure S6). Both proteins could be observed localizing to the LDs, as well as in the cytosol, both in normal media or upon addition of oleic acid to promote LD formation. We therefore conclude that the presence of an increased number of identical repeats in mutant PLIN4 promotes its aggregation without significantly impacting its interaction with LDs.

Influence of lipid droplets on PLIN4 fibril formation

Previous work has shown that the repetitive region of PLIN4 binds to LDs via the formation of an amphipathic helix, and is required for PLIN4 targeting to LDs in cells [22]. We have also shown that LD binding affinity increases with the number of repeats, suggesting a velcro-type mechanism of LD binding. Interestingly, the PLIN4 repetitive regions binds much more readily to LDs than to bilayer membranes because it favors interaction with the neutral lipids of the LD core compared to the phospholipid surface (Figure 4A) [22,33].This same repetitive region of PLIN4 is expanded in myopathy patients and forms amyloid fibrils *in vitro.* We therefore wanted to assess how the presence of LDs affects PLIN4 fibril formation. We prepared artificial LDs composed of triglycerides, which form the neutral lipid core, and phosphatidylcholine (PC), the most abundant phospholipid forming the LD surface monolayer [49]. In order to prepare a homogenous suspension of artificial LDs, we adjusted their density to be close to the density of water solution by the addition of brominated oil, following a recently-established protocol [33]. Binding of purified perilipins, including PLIN4-12mer to these artificial LDs can be assessed by fluorescent microscopy or by other approaches, as has been described by Araújo et al. (2024). We therefore included in the LD preparation a small amount of fluorescently-labelled phospholipid (rhodamine-conjugated phosphatidylethanolamine; rhodamine-PE) in order to visualize the LDs by fluorescent microscopy. Incubation of these dense LDs with fluorescently-labelled PLIN4-12mer[260:] or 12merMUT showed that both proteins could bind to the LD surface, especially after a prolonged incubation of 24h at room temp. (Figure 4B).

Next, we performed a ThT aggregation assay with 4mer[260:], 12mer[260:] or 12merMUT in the presence of an increasing concentration of LDs, from 0 to maximum possible. To compare the influence of LDs on the aggregation of different PLIN4 constructs, we calculated the LD to protein ratio in the different reactions by using the molar PC concentration as a measure of available LD surface, normalizing this to the total molar concentration of 33-aa repeats (mer) in each reaction (Figure 4C). The aggregation of 4mer[260:] or 12mer[260:] was slowed-down or completely blocked, respectively, by an increasing concentration of LDs (Figure 4C). By contrast, the aggregation of 12merMUT was much less affected by LDs at the same PC (surface lipid) to protein molar ratio (Figure 4C, right-most panel). Furthermore, PC liposomes (bilayer membranes) had less effect on aggregation of 4mer[260:] or of 12merMUT compared to LDs, event at a >100-fold higher PC concentration. This result correlates with a lower affinity of PLIN4 amphipathic helix for

bilayers compared to LDs (Figure S7A-C) [22,33]. We therefore conclude that aggregation of the PLIN4 repetitive region may be slowed down by LDs via a competitive mechanism: for WT PLIN4 repetitive region, binding to LDs is more pronounced than aggregation, whereas in the case of PLIN4-12merMUT, aggregation is less sensitive to the presence of LDs, likely because aggregation occurs faster than LD binding.

Identical repeats of PLIN4 promote aggregation in a yeast model

Finally, we wanted to establish an orthogonal model to evaluate the effect of PLIN4 sequence on the aggregation of the PLIN4 repetitive region. The budding yeast has been shown to be a useful model to study the interaction of perilipins with LDs, and the PLIN4 repetitive region interacts with LDs in a similar manner as in human cells [22,35,50,51]. Budding yeast has also been a useful model for studying the aggregation of different human proteins [52–55]. We therefore used this model to analyze the influence of identical repeats on PLIN4 aggregation. We expressed in yeast two PLIN4 12-mer fragments, 12mer[260:] and 12merMUT, both from a high expression GPD promotor [56]. Expression of the two fragments, fused to mScarlet, did not affect the growth of wild-type yeast (Figure 5A). As observed previously with 12mer[524:] at lower level of expression after 24h growth to stationary phase, whereby LDs accumulate [22], 12mer[260:] localized to LDs as well as to the plasma membrane (PM), in addition to displaying soluble cytosolic signal. By contrast, 12merMUT was predominantly cytosolic under these conditions (Figure 5B). However, after prolonged incubation (48 h of growth), with LDs further increasing in size, both constructs could be observed on LDs. We conclude that both 12mer fragments can localize to LDs, in accordance with the *in vitro* results showing that both constructs can interact with LDs. However, the affinity of 12merMUT for LDs seems decreased, compared to the WT version 12mer[260:].

To determine whether PLIN4-12mer[260:] or PLIN4-12merMUT form aggregates within yeast cells, we used a strain expressing the heat shock protein Hsp104, tagged with GFP in the chromosome. Hsp104 is a protein disaggregase, commonly used as a marker of protein aggregates [52,57]. Using different growth conditions, we could consistently observe large puncta of 12merMUT in a fraction of yeast when they were grown for 18h to the start of diauxic shift (Figure 5A & 5C). While infrequent, these puncta always colocalized with Hsp104-GFP, suggesting that they represent protein aggregates. By contrast, such puncta were never observed in yeast expressing PLIN4-12mer[260:] (Figure 5D). Therefore, these results show a clear and reproducible difference in the behavior of the two PLIN4 fragments and indicate that identical repeats, present in 9 copies in PLIN4-12mer[MUT], compared to 3 copies in 12mer[260:], promote aggregation. The decrease in affinity of PLIN4-12merMUT for LDs, compared to 12mer[260:], could also contribute to its increased aggregation. Unexpectedly, we did not observe a more pronounced accumulation of 12merMUT aggregates upon prolonged incubation of yeast cultures, which may indicate clearance of aggregates by the cells.

Based on our experiments *in vitro* and in the yeast model, we conclude that the repetitive region of PLIN4 possesses an intrinsic propensity to aggregate via formation of amyloid fibrils, which is promoted by the presence of identical 33-aa repeats.

Discussion

Many degenerative diseases are linked to protein misfolding and amyloid deposits in affected tissues. The identity of the protein and the 3D structure of the protein deposit are intimately linked to each specific disease [6,58]. Here, we show that the LD-binding protein PLIN4 is a novel protein capable of forming amyloid fibrils, as confirmed by cryo-EM of the purified PLIN4 repetitive region. We further show that, compared to the wild-type PLIN4 repetitive sequence, aggregation is greatly promoted by multiplication of identical 33-aa repeats within the PLIN4 repetitive region present in the MRUPAV vacuolar myopathy patients [19]. Our *in vitro* analysis suggests that rather than the increase in length of the repetitive region, it is the accumulation of identical repeats in the mutant sequence that is the most efficient in promoting aggregation, raising important implications for the general mechanism of amyloid fibril assembly. Furthermore, we show that LDs inhibit PLIN4 aggregation *in vitro*, suggesting that LDs could act as a buffer to decrease the propensity of PLIN4 to aggregate, raising the possibility that tissue-specific or diet-dependent differences in lipid metabolism may play an important role in modulating PLIN4 aggregation in cells. Based on our results, we propose that the genetic expansion in *PLIN4* represents a toxic gain-of-function mutation, which, by promoting PLIN4 aggregation, interferes with muscle fiber contraction.

There are other known examples of proteins that aggregate within muscle fibrils, causing disease; for example, myofibrillar myopathies, which often include aggregates of desmin – a muscle-specific intermediate filament [17,59]. The fibrils formed by desmin are also likely to be amyloid in nature. As in the case of other amyloid-forming proteins implicated in degenerative disease, the mechanisms by which these proteins are toxic to cells are not well understood. In the case of PLIN4, accumulation of the protein has been observed in skeletal muscle of patients carrying the *PLIN4* expansion, in particular within the vacuoles, where PLIN4 puncti colocalize with p62 and other aggrephagy markers [18,19,24,25].

Our kinetic assays suggest that the disease expansion in PLIN4 may strongly promote amyloid formation via intramolecular stacking of identical repeats, although this needs to be verified by high-resolution structural analysis. The identical-repeat constructs show rapid aggregation at lower concentration than the WT sequence. However, structural analysis of the resulting aggregates is hampered by their large size and amorphous shape, likely a consequence of rapid growth. Nevertheless, the model of intramolecular stacking is enticing. Only a few such examples have been described to date. One is the fungal protein Het-S, which forms cell-death inducing functional amyloids that are formed by a stack of two imperfect repeats of 21 aa within the same molecule [60,61]. The other known examples are the bacterial functional amyloids curli involved in biofilm formation, present in many Gram-negative bacteria, including in *Escherichia coli* (CsgA). In these cases, amyloid fibrils contain intra-molecular stacks composed of a variable number of multiple imperfect repeats; up to 16 have been observed so far [62–64]. Stacking of multiple units within the same molecule would therefore represent a novel type of amyloid fibril architecture implicated in a degenerative disease.

PLIN4 display a particularly huge number of imperfect 33 aa repeats, spanning over 1000 residues. While our results indicate that alone a number of individual repeats can assemble into filaments,

the variable residues within different repeats could represent anti-aggregation residues. For example, it has been shown that the presence of "gate-keeper" residues within a few central repeats in CsgA reduces amyloid formation [65,66]; similarly, the presence of specific flanking sequences can inhibit the aggregation of polyglutamine repeats [67]. The presence of identical repeats in PLIN4 mutant may abolish the anti-aggregation properties of flanking repeats. These considerations also suggest strategies for inhibiting PLIN4 aggregation by the use of interfering peptide [65,68]. *In vitro*, we have studied amyloid formation using fragments ranging from 33 aa (single repeat) to 396 aa (12 x 33-aa repeats), and up to 660 aa (PLIN4-20mer), which represent very large protein fragments for precise kinetic and structural studies. Although we do not expect that the N- and C-terminal segments of PLIN4 directly participate in amyloid formation, it will be important to understand how they affect PLIN4 aggregation properties. Analyses of highly-studied amyloid forming proteins like tau and α-synuclein show that flanking regions crucially affect the properties of amyloid fibrils, leading to diverse structures that can be linked to different disease phenotypes [8]. Studying the aggregation of full-length PLIN4 will be an important challenge for future work.

Although PLIN4 is the first example of a *bona fide* LD protein forming amyloids, many disease-related amyloid-forming proteins interact with lipid membranes, which likely play an important role in the disease pathology [38,40]. Degenerative diseases are often linked to defects in cellular lipid metabolism and changes in membrane lipid composition brought upon by the process of ageing [69,70]. Different lipids promote or inhibit aggregation or amyloid formation of amyloid-β or α-synuclein [37,53,71–73]. In cells of Parkinson's and Alzheimer's models, LDs and other lipid-bound organelles have been observed in proximity of amyloids [38,40]. LDs have been suggested to act as a buffer for toxic protein aggregates and were shown to suppress lipotoxic effects associated with Parkinson's disease and other degenerative disorders [39]. Moreover, recent studies have demonstrated that lipids can be incorporated into amyloid-β or α-synuclein amyloid fibrils thus changing their structure and properties [71,74]. We suggest that PLIN4 provides a favorable context to connect *in vitro* studies performed using pure proteins and lipids to cellular investigations and to pathology in organisms.

In adipocytes, we have recently shown that PLIN4 is particularly well adapted to handling fast forming LDs [33]. In muscle, it is known that LDs are abundant within the myofibers and play an important role in muscle contraction. Interestingly, LD size, number and distribution, in particular their association with mitochondria, change with training, ageing and also in type-II diabetic patients [28,29]. Thus, the fact that PLIN4 aggregation occurs in skeletal muscle, whereas the function of the adipose tissue does not appear to be affected in MRUPAV patients, suggests that differences in lipid metabolism between the two tissues might favor or disfavor PLIN4 aggregation versus its normal function on LDs. In the brain, the balance between lipid metabolism and protein aggregation is difficult to study (e.g. for α-synuclein) because this organ is extremely stable in lipid composition [75]. In contrast, muscles and adipose tissues are prone to rapid changes in lipid composition owing to diet-induced changes [28,76]. Therefore, understanding the interplay between PLIN4 binding to LDs and its propensity to aggregate in cells will not only be essential for defining the role of PLIN4 in the MRUPAV vacuolar myopathy, but will also bring insight into other degenerative diseases linked to LDs and changes in lipid metabolism.

In conclusion, we report here that the LD-binding protein PLIN4 is a novel amyloid-forming protein and we propose that the genetic expansion in *PLIN4* present in patients suffering from a recently-discovered vacuolar myopathy (MRUPAV) promotes amyloid formation at the origin of cellular disfunction. Furthermore, we show how small variations in the sequence of PLIN4 33-aa repeats can drastically increase or decrease the propensity to form amyloid fibrils. According to currently available data, MRUPAV is an extremely rare genetic disease, with only 4 families and one sporadic case having been reported world-wide [19,24,25]. However, due to highly similar repeats of 99 bp present in *PLIN4,* genetic expansions in this region cannot be identified by the high-throughput screening approaches routinely used in the diagnostic practice. By screening biopsy samples of vacuolar myopathy patients with an unknown genetic cause, A Ruggieri and colleagues have already identified another patient with a different expansion in *PLIN4* within their cohort (Carnazzi et al., manuscript submitted), therefore suggesting that *PLIN4* expansions are more common. Furthermore, two new families with two different numbers of additional PLIN4 repeats have been described in a conference proceedings [77]. These considerations suggest that toxic expansions in *PLIN4* may be considerably more common, underlying the importance of understanding the molecular mechanism of PLIN4 aggregation, which can lead to development of therapies for affected patients.

Resource availability

All unique/stable reagents generated in this study are avail-able from the Lead Contact with a completed Materials Transfer Agreement.

Acknowledgments

We thank Manuel Giménez Andrès for assistance with protein purification and labelling, Amel Balhoul for help with CD spectroscopy, Laura Picas for advice on the AFM experiments, Véronique Albanèse for advice and plasmids for yeast experiments, and Bruno Antonny, Andrey Kajava and Dimitris Xirodimas for helpful discussions and comments on the manuscript. This work benefited from the CryoEM platform of I2BC, supported by the French Infrastructure for Integrated Structural Biology (FRISBI) [ANR-10-INSB-05-05], the MRI imaging facility, a member of the national infrastructure France-BioImaging, supported by the French National Research Agency (ANR-10-INBS-04, Investissements d'avenir), the joint IGMM-CRBM "yeast media and technologies service", and the Synbio3 platform (IBMM, Montpellier University, France), supported by GIS IBISA. The NanoImaging Core at Institut Pasteur is acknowledged for support with sample preparation, image acquisition and analysis. The NanoImaging Core was created with the help of a grant from the French Government's Investissements d'Avenir program (EQUIPEX CACSICE - Centre d'analyse de systèmes complexes dans les environnements complexes, ANR-11-EQPX-0008). This work was supported by the European Research Council (ERC Synergy 856404, SPHERES), the Agence Nationale de la Recherche (ANR-23-CE44-0026) and by AFM Téléthon (SR 2024 #289888).

Author contributions

Conceptualization: A.C., A.R. and L.B.; Data curation: N.F., C.M., C.F., S.L., L.B., A.C.; Formal analysis: C.C., S.L. and L.B.; Funding acquisition: A.C., A.R. and L.B.; Investigation: C.C., N.F., B.S., C.M., C.F., S.L., T.P., S.P., L.B., A.C.; Methodology: N.F., C.M., S.L., L.B., A.R., A.C.: Project administration: A.C., Resources: C.M., A.R, and S.R., Supervision: A.C., L.B., S.L.; Visualization: C.C., N.F., B.S., C.M., C.F., S.L., L.B.; Writing – original draft: A.C.; Writing – review & editing: L.B., C.C., N.F. C.M., and A.R.

Declaration of interests

The authors declare no competing interests.

Supplemental information

Document S1. Table S1, Figures S1-S7.
Table S2. Excel file containing descriptions, amino acid and DNA sequences for all proteins and peptides used in this study, related to Key Resources Table.
Table S3. Excel file containing DNA and transcribed amino acid sequences of synthetic genes used for construction of mammalian PLIN4 expression plasmids.

Figure Legends

Figure 1. PLIN4 repetitive regions is prone to formation of fibrils.
(A) Schematic representation of human PLIN4 (Uniprot Q96Q06), with the repetitive region 29 x 33 aa repeats shown in red, and the predicted 4-helix bundle domain in blue. The positions of the constructs 12mer[260:], 12mer[524:] and 20mer, containing 12 or 20 repeats, are indicated, as well as the genetically-encoded expansion in MRUPAV patients [19].
(B) Thioflavin T (ThT) assay to monitor the aggregation kinetics over 90 hours (h) of 12mer[260:] at 1 mg/mL (red), 0.5 mg/mL (orange) and 0.25 mg/mL (green) and 12mer[524:] at 1 mg/mL (purple).
(C) Pelleting assay (left) of 12mer[260:] and 12mer[524:] at 0.25 mg/mL and 1 mg/mL before and after the ThT assay carried out for 100 h (right). Pellets and supernatants after centrifugation at 100 000 g were analyzed by SDS PAGE and stained with GelcodeBlue.
(D) Fibrils obtained by aggregation of 12mer[260:] at 0.5 mg/ml in a ThT assay were visualized by negative stain EM. Scale bar: 0.2 µm.
(F) CD spectra of 12mer[260:] (above) and 12mer[524:] (below) (13 µM and 14 µM, respectively) in buffer or in the presence of 50% TFE.

(G) Limited proteolysis of 12mer[260:] (above) and 12mer[524:] (below) (0.1 mg/ml for both proteins) with 0.2 µg/mL subtilisin, in the presence or absence of liposomes. Proteins were analyzed by SDS-PAGE and stained with Silver stain. Data shown is representative of 2-3 independent experiments.

Figure 2. PLIN4 fibrils are amyloid in nature.
(A) Fibrils formed from Plin4-12mer[260:] observed by cryo-EM. Scale bar: 100 nm.
(B and C) 2D classification of Plin4-12mer[260:] using Relion. Representative 2D classes using 1350 Å box size binned to 3.85 Å/pixel, which identifies two polymorphs with a thick diameter (B, left panel) and thin diameter (C, left panel). Middle panels: 2D classification of the thick and thin polymorph with un-binned images (0.77 Å/pixel) revealing a typical amyloid spacing. Right panels: Fourrier transform of the 2D class shows a strong reflection at 4.79 Å for both thick and thin polymorphs.
(D) Plin4-12mer[260:] fibrils formed from Plin4-12mer[260:] were deposited onto freshly cleaved mica and imaged in buffer in PeakForce tapping mode AFM (scale bar: 250 nm). The right panel is a high resolution magnification of the fibril in the white box, highlighting the twist pattern (scale bar: 100 nm).
(E) Straightened fibril and its corresponding height profile, showing a periodicity in the height profile of a single fibril. The approximal length of the repeating unit between two height maxima (periodicity) is indicated.
(F) Distribution of periodicities measured for about 15 different fibrils, as shown in (E); each dot is the measurement of one periodicity (n=50).
(G) Multiple scans were recorded every two minutes on a single fibril, resulting in fibril breakage (scale bar: 250 nm). In the 3rd upper panel, recorded at 6 min, the arrows indicate punctual distortion of the fibrils before breaking (boxed area at 8 min). The lower panels show a 2.5x magnification (scale bar: 100 nm) of the same area that is shown in the box at 8 min containing the breakage site, at 10, 12 and 14 min. The right-most bottom image shows an 2x magnification of the broken fibril in the white box at 14 min, with arrows indicating height profiles of the visible structures (scale bar: 50 nm).

Figure 3. The influence of PLIN4 repeat sequence and number of repeats on aggregation.
(A) Diagram of PLIN4 showing %identity between individual 33-aa repeats compared to repeat 6 (r6 = 1mer[260:]), which is multiplied in patients, as a heat map score. Color scale: from 42,4% identity in yellow (minimum %identity) to 100% identity score in red (see Table S1). The expanded region is composed of 3 strictly identical repeats. Represented below: 4mer and 12mer constructs from the WT sequence (containing 3 identical repeats), and the 12mer[260:]MUT construct with 9 identical repeats.
(B) Weblogo [78] showing conservation between the 29 33-aa repeats present in WT PLIN4.
(C) Heat map scoring of the amyloidogenic propensity of individual 33-aa repeats, determined by ArchCandy (see Table S1). The positions of the three 33-aa peptides that were evaluated experimentally, 1mer[260:], 1mer[642] and 1mer[741], are shown below.
(D) Aggregation kinetics in the ThT assay of the peptides representing single 33-aa repeats, 1mer[260:], 1mer[642:] and 1mer[741:], at 1 mg/mL (red), 0.5 mg/mL (orange) and 0.25 mg/mL (green).

(E) Aggregation kinetics in the ThT assay of 4mer[260:] at 0.5 mg/mL (orange) and 0.25 mg/mL (green).
(F) Aggregation kinetics in the ThT assay of 12mer[260:], compared to 12mer[260:]MUT at 1 mg/mL (red), 0.5 mg/mL (orange), 0.25 mg/mL (deep green) and 0.125mg/mL (light green).
(G) ThT aggregation kinetics of MBP constructs containing 2, 3 or 4 tandem identical repeats of the 33-aa sequence 1mer[260:], in the presence (pink to red) or absence (blue) of TEV protease. Two or three different concentrations were tested for each protein (1X, 2X or 3X), with some variability in the 1X concentration: MBP-2x1mer[260:] = 0.4 mg/mL; MBP-3x1mer[260:] = 0.5 mg/mL; MBP-4x1mer[260:] = 0.55 mg/mL. Proteins were tested immediately after purification without freeze-thawing to minimize protein degradation.
(H) Reaction mixtures after ThT aggregation were analyzed by negative stain EM. Fibrils were detected only in the 4x1mer[260:] samples + TEV (upper panel) and – TEV (lower panel). Scale bar: 1 µm or 0.5 µm for the magnified area (2 x zoom).
(I) Model of intermolecular vs. intramolecular amyloid stacking.

Figure 4. The influence of LDs on PLIN4 aggregation in vitro.
(A) Schematic model of the different states of the PLIN4 repetitive region. The same region can interact with LDs or, more weakly, with lipid bilayers [22,33], or form amyloid fibrils.
(B) Binding of 12mer[260:] or 12merMUT, labelled with AlexFluor488, to artificial LDs containing Rhodamine-PE was observed by confocal microscopy immediately or after a 24-hour incubation at RT. Scale bar: 10 µm.
(C) ThT aggregation assay of 4mer[260:] (0.125 mg/mL), 12mer[260:] (1 mg/mL) and 12merMUT (0.125 mg/mL) in the presence of artificial LDs at the indicated lipid to protein molar ratio, expressed as the ratio of PC in the LD surface monolayer to 33-aa repeat for each construct. The exact ratios are presented with a color scale and indicated on the right side of each graph. Protein concentrations were chosen such as to obtain good aggregation in the absence of LDs. See also Figure S6 for comparison of aggregation in the presence of liposomes.

Figure 5. Analysis of PLIN4 aggregation in the budding yeast model.
(A) Growth curves of yeast strains containing either an empty plasmid, or a plasmid expressing the indicated construct.
(B) Localization of PLIN4-12mer[260:] and PLIN4-12merMUT-mScarlet fusion proteins in aged cells that accumulate LDs (stained with AutoDOT; right panels), after 24h and 48h incubation at 30°C, as indicated. Bottom rows for each construct show a 3x zoom-in of the indicated area. Scale bar: 5 µm.
(C) Localization of 12mer[260:] and 12merMUT-mScarlet fusion proteins in yeast with endogenously-tagged Hsp104-GFP. Cells were grown for 18h in SD-Ura medium at 30°C prior to observation, and LDs were stained with AutoDOT. Scale bar: 5 µm.
(D) Quantification of the percent of cells with observable PLIN4-12mer aggregates that colocalize with Hsp104-GFP, as shown in (C). Each colour symbol on the graph represents an independent experiment. Cell counts for were 12merMUT: Blue, n=7298, Green, n=20958, and Purple, n=10092, and for 12mer[260:]: Blue, n=8753, Green, n=32275, and Purple, n=7569. The value for 12mer[260:] was 0 in all experiments.

STAR Methods

Key Resources Table

Protein sequence analysis

The Uniprot entry Q96Q06 was used as the default sequence for human PLIN4. The aa repeats were identified using HHrepID rom the MPI Bioinformatics Toolkit as previously described [35,79]. Repeats were aligned using AlignmentViewer (http://alignmentviewer.org) and the repeat alignment was presented using Weblogo [78]. The TAPASS pipeline [46], including amyloid prediction algorithms ArchCandy2, Pasta and Tango (Ahmed et al., 2015; Fernandez-Escamilla et al., 2004; Walsh et al., 2014), was used to identify the ARs within the PLIN4 sequence. The amyloidogenic score of individual 33-aa repeats was determined using ArchCandy2.

Cloning and plasmid construction for protein purification

All purified PLIN4-derived proteins were expressed from pET21b (Novagen)-based plasmids constructed using synthetic genes encoding human sequence (Uniprot entry Q96Q06), codon-optimized for human PLIN4 and to reduce the percent of sequence identity, ordered from Eurofins (designed using the Eurofins algorithm). All PLIN4-4mer and PLIN4-12mer sequences were subcloned into pET21b using NheI and HindIII restriction sites, to be expressed without an N-ter or a C-ter tag. The only exception was PLIN4-4mer[260:], which was inserted into pET21b digested with BamH & HindIII, preserving the N-ter T7 tag of 13 aa (1.4 kDa). PLIN4-20mer was cloned into pET21b as previously described (Copic et al., 2018), for expression and purification without a tag. PLIN4-1mer synthetic peptides were ordered from Proteogenix. To produce the MBP-PLIN4-1mer[260:] fusion proteins, the indicated number of PLIN4-1mer[260:] repeats (2, 3 or 4) were amplified by PCR from plasmid pCC05, and inserted into the pETM40 bacterial expression vector using NcoI/StuI restriction site to produce in-frame fusion with a 5' MBP tag-encoding sequence, followed by the TEV protease cleavage site (5'-GAGAATCTTTATTTTCAGGGC-3'). All proteins and peptides used in this study are described in detail in Table S2, and the names of plasmids used for their purification are provided.

Yeast plasmids, growth and media

To construct plasmids for expression of PLIN4-12mer[260:] (pCM86) and PLIN4-12merMUT (pCM85) in budding yeast, sequences indicated in Table S2 (codon-optimized for humans) were subcloned by Gibson cloning into a pRS416 (*CEN, URA3*, Amp^R) plasmid containing the strong GPD promoter [56]. They were then tagged at the C-termini with a mScarlet fluorescent protein (amplified from pBBK83, addgene #179067) by Gibson cloning (Linker sequence: GSGPSGPTG). The yeast strain used for all experiments was BY4741 MATa his3Δ1 leu2Δ0 met15Δ0 ura3Δ0 *HSP104::GFP::HygrMX*. The GFP-coding cassette [80] was inserted at the 3' end of *HSP104* by homologous recombination and verified by fluorescent microscopy. Yeast cells were grown in yeast extract/peptone/glucose (YPD) rich medium, or in synthetic complete (SC) medium containing 2% glucose. Yeast was transformed by standard lithium acetate/polyethylene glycol method. For observation of aggregates, liquid cell cultures were inoculated from a single colony and grown for 18 h at 30 °C in SC-Ura with 2% glucose to maintain plasmid selection and observed directly by confocal microscopy. For observation of LDs, yeast were grown under the same growth

conditions for 24h or 48h. LDs were stained with AutoDOT (CliniScience) for 20 min at room temp in growth medium and the cells were washed twice before observation.

Plasmids for mammalian cell culture

Plasmids for stable expression of full length wild-type PLIN4 (pSB-PLIN4-WT-GFP, pSR002) or PLIN4 mutant (pSB-PLIN4-MUT-GFP, pSR003) in HeLa cells were constructed using the Sleeping Beauty (SB) transposon system [81]. Four synthetic genes (GeneArt Gene Synthesis, Thermo Fisher Scientific), listed in Table S3 (pSG-Nter, pSG-RPT1, pSG-RPT2, pSG-Cter-GFP), encoding codon-optimized human PLIN4 and encompassing the entire wild-type sequence with a C-terminal GFP tag, were assembled using the NEBuilder DNA HiFi assembly kit (New England Biolabs). The resulting construct was cloned into the pSBtet-Pur vector (a gift from Eric Kowarz, Addgene plasmid#60507). The PLIN4 mutant construct was generated from the wild-type sequence by inserting the repeat expansion (pSG-12mer-id, see Table S3) using the same NEBuilder system and cloned into the same vector. Plasmids were verified by sequencing.

Establishment of inducible stable cell lines

HeLa cells were grown in Dulbecco's modifiedEagle's medium (DMEM) supplemented with 4.5 g l−1 glucose (Life technologies), 10% fetal bovine serum (FBS, Life technology) and 1% Penicillin/Streptomycin antibiotics (Life technologies). Sub-confluent cells were co-transfected with plasmids encoding either pSB-PLIN4-WT-GFP (pSR002) or pSB-PLIN4-MUT-GFP (pSR003), along with the Sleeping Beauty transposase SB100X (pCMV(CAT)T7-SB100; a gift from Zsuzsanna Izsvak, Addgene plasmid # 34879) [82] using Fugene HD in Optimem medium (Life technologies). Twenty-four hours post-transfection, stable integrants were selected in tetracycline-depleted medium supplemented with puromycin (1 µg/mL). Inducible expression of the transgenes was triggered by adding doxycycline (1 µg/mL) overnight and confirmed *via* Western blot analysis and immunofluorescence microscopy. For observation by confocal fluorescent microscopy, stable transfected cells were induced with doxycycline (1 µg/mL) overnight in standard growth medium or standard growth medium containing 150 µM oleic acid (Sigma) in complex with fatty-acid free BSA (Sigma). LDs were stained with Lipi-Blue (0.1 µmol/L, Dojindo) for 30 min in the standard growth medium without phenol red immediately prior to live imaging by confocal microscopy.

Protein expression and purification

All proteins and peptides used in this study are listed in Table S2. The recombinant PLIN4-20mer, PLIN4-12mer[260:], PLIN4-12mer[524:], PLIN4-12merMUT, PLIN4-4mer[260:], PLIN4-4mer[326:], PLIN4-4mer[557:] and PLIN4-4mer[689:] proteins were purified without a tag following a previously-established procedure [22]. They were expressed in *E. coli* BL21(DE3) at 37°C for 1 h 40 min after induction with 1mM IPTG (at OD_{600} = 0.6-0.8). Always at 4°C, cells were lysed in lysis buffer A (20 mM Tris-HCl pH 7.5, 10mM NaCl, 1mM dithiothreitol (DTT), 5mM PMSF, protease inhibitors tablet cOmplete; Roche) by sonication (amplification 40%, 10 sec ON, 20 sec OFF 10 times) and the lysates were centrifuged at 40,000 g for 30 min. Boiling step of the supernatants at 95°C was performed for 30 min in a water bath, followed by 10 min in ice and centrifugation at 40,000 g for 20 min. 2 rounds of dialysis (90 min each) were performed against lysis buffer B (20 mM Tris-HCl pH 7.5, 10 mM NaCl, 1 mM TCEP) using Spectra/Por membranes with a cut off of 6000 Da (Spectrum labs), followed by 30 minutes of centrifugation at 40,000 g. Purification was

performed on a NGC FPLC system (BioRad), using a Hiprep SP 16/10 cation-exchange column (Cytiva). Proteins were eluted with a linear salt gradient with elution buffer B (20 mM Tris-HCl pH 7.5, 1M NaCl, 1mM TCEP) and protein-containing fractions were pooled, aliquoted for single use and stored at -80°C. Protein concentration was determined by densitometry from SDS-PAGE gels stained with GelCodeBlue (Thermofisher) using bovine serum albumin (BSA) standards for calibration. Note that due to the lack of aromatic residues in the PLIN4 repetitive region, protein concentration cannot be determined by standard assays such as Bradford; for details see [22].
MBP-fusion proteins containing PLIN4-1mer[260:] repeats (2, 3 or 4, as indicated) were expressed in *E. Coli* Arctic (DE3) cells at 18°C overnight following induction with 1mM IPTG (at OD_{600} = 0.6-0.8). Cells were lysed by sonication in lysis buffer A (20 mM Tris-HCl pH7.5, 50 mM NaCl), supplemented with 10% glycerol, 1 mM TCEP, 1 mM EDTA, 0.5 mM PMSF, 1.5 µM pestatin, 2 µM bestatin and a protease inhibitors coctail cOmplete (Roche), as described above, and centrifuged to produce cleared lysates. The lysates were incubated for 2 h at 4°C under rotation with amylose beads and then sequentially eluted with 1 mL of maltose elution buffer (lysis buffer supplemented with 50 mM maltose). Elution fractions 1 and 2 were pooled together and immediately used in the ThT aggregation assay (immediate use without freeze-thawing was essential to reduce protein degradation). Protein concentration in the eluted fractions was determined by densitometry from SDS-PAGE gels stained with GelCodeBlue using bovine serum albumin (BSA) standards applied on the same gel for calibration. Similar protein concentrations were obtained with the different MBP-constructs, as indicated in the figure legends. TEV (Tobaco Etch Virus) protease was purified in-house and added to the ThT assays at the same time as the MBP-fusion proteins at a concentration of 0.05 mg/mL, when idicated.

Protein fluorescent labelling

Purified PLIN4 fragments were labelled via endogenous cysteines using Alexa Fluor 488 C5 maleimide dyes (ThermoFisher), as previously described [22]. Briefly, for proteins purified in the presence of DTT, they were first dialyzed on a NAP10 desalting column (Cytiva) against 50 mM Tris-HCl pH 7.5, 120 mM NaCl buffer The reactions were carried out with 5-fold molar excess (per Cys) of the dye for 20 min at 4°C, then blocked with 2mM DTT. The free dye was removed using desalting NAP-5 columns (Cytiva) equilibrated with 50 mM Tris-HCl pH 7.5, 120 mM NaCl buffer, supplemented with 2 mM DTT. The fractions were analyzed by SDS-PAGE and UV-visible chromatography. Labeled proteins were stored at -80°C in small aliquots and mixed with a 5-fold excess of identical unlabeled protein when needed.

Synthetic peptides

Unmodified synthetic peptides of 33 aa were ordered from Proteogenix. They were stored in 1 mg aliquots at -20°C and dissolved in dH_2O or in 25 mM Tris, pH 7.5, 100 mM NaCl just before use.

ThT aggregation assay

Immediately prior to an aggregation assay, in order to remove any aggregation seeds (oligomers or pre-formed fibrils), all proteins and synthetic peptides were centrifuged at 100,000 g for 1 h at 4°C. Aggregation was performed in 25 mM Tris, pH 7.5, 100 mM NaCl and 1 mM DTT (freshly added), supplemented with 15 µM Thioflavin T. The reaction mixtures (250 µl) were pipetted into wells of a Greiner BlackPlate 96 Flat containing one 2 mm glass bead per well and sealed with a

plastic seal (ref). Fluorescence was monitored continuously every 10 min in a TECAN SPARK fluorescent plate reader at 37°C, with orbital shaking for 300 s, amplitude of 2.5 mm and frequency of 216 rpm. Thioflavin T fluorescence was acquired in the top reading mode at 2x2 multiple reads per well, with a 430/485 nm filter, 40 % manual gain, 50 % mirror, 30 flashes and 40 µs of integration flash, at an optimized Z-Position (usually around 18500 µm). After aggregation curves reached a plateau, samples were removed from the plate and stored in low-binding Eppendorf tubes in the dark at room temperature.

Protein pelleting assay

When the ThT fluorescence signal of aggregation assays with different PLIN4 constructs reached the plateau, 50 µL of each reaction was centrifuged at 40 K rpm for 30 min at 25°C. Supernatants were collected and mixed with 2x Laemmli buffer containing 5 mM DTT, and pellets were resuspended in 100 µl of the 1x Laemmli buffer with DTT. Equal volume (10 µl) of each sample was loaded on a 17% SDS polyacrylamide gel and analyzed by SDS polyagrylamide gel electrophoresis (SDS PAGE) in Tris-glycine migration buffer containing 0.05% SDS. Proteins were stained using GelCode Blue (Thermo Scientific).

Circular Dichroism

The experiments were conducted on a Jasco J-815 spectrometer at room temperature with a quartz cell of 0.05 cm path length. Each spectrum is the average of several scans recorded from 200 to 260 nm, with a bandwidth of 1 nm, a step size of 0.5 nm, and a scan speed of 50 nm/min. Control spectra of 50 mM Tris, pH 7.5, and 150 mM NaCl buffer without or with 50% TFE were subtracted from the protein spectra.

Negative stain EM

Negative stain EM of amyloid fibrils was performed as described [83]. Briefly, PLIN4 samples were diluted to 0.1 mg/mL in MilliQ water. Glow discharged carbon coated 400 mesh copper grids were floated over 30 µL drop for 1 min. The excess of liquid was absorbed on Whatman filter paper, and the grid was stained for 1 min over a 30 µL droplet of 1% uranyl acetate. The grids were observed under Jeol 1400 electron microscope at 80 kV and 10 K magnification, images were recorded on a Gatan Rios CCD camera with automatic drift correction.

Cryo-EM

PLIN4-12mer[246] filament preparations were screened by negative stain EM to identify the most homogenous samples suitable for Cryo-EM. Quantifoil R3.5/1 grids were prepared using 3µl of 1mg/ml plin4 sample using a Vitrobot. Data collection on Titan KRIOS equipped with Falcon 4i camera at the Institut Pasteur. 6000 images were acquired with a 0.77 Å pixel size and defocus ranging from 0.4 to 2.5 µm. All data were processed with Relion4 [84] for 3D classification using a 1024x1024 pixel box size binned to 256, or an unbinned 350x350 pixel box size to detect the 4.7 Å spacing.

Atomic force microscopy

AFM experiments were done using a JPK NanoWizard IV xp microscope (Bruker nano GmbH, Germany) using the PeakForce tapping mode in liquid and PeakForce-HIRS-F-B probes (nominal

tip radius = 1 nm, nominal spring constant 0.1 N/m, Bruker). PLIN4-12m[260:] fibrils [1 - 2 mg/mL], collected after Thioflavin T assay, were diluted ten times then incubated for 10 min on freshly cleaved mica surface before imaging in buffer (25 mM Tris, pH 7.5, 100 mM NaCl). 256 x 256 pixels images were collected at scan rate of 5Hz, with a PeakForce setpoint of 300pN and Z-Range of 7.5 µm. JPK data analysis software (version 8.0.177) was used to process the image data by flattening the height topology and to measure manually the periodicity from the height profile.

Lipids

DOPC (1,2-dioleoyl-sn-glycero-3-phosphocholine), diphytanoyl-PC (1,2-diphytanoyl-sn-glycero-3-phosphocholine), diphytanoyl-PS (1,2-diphytanoyl-sn-glycero-3-phospho-L-serine) and Rhodamine-PE (L-α-Phosphatidylethanolamine-N-(lissamine rhodamine B sulfonyl) were purchased from Avanti Polar Lipids as chloroform solutions. Triolein (1,2,3-tri-(9Z-octadecenoyl)-glycerol) and BVO (Brominated Vegetal Oil, CAS: 8016-94-2) were purchased from Sigma-Aldrich and Spectrum Chemical MFG Corp, respectively. BVO was purified before use as described [33]. Lipids were stored as chloroform stock solutions at -20°C under argon.

Liposome preparation

Phospholipids in chloroform were mixed at the desired molar ratio and dried under argon flux. To prepare fluorescently-labeled liposomes, 0.1 % of Rhodamine-PE was included in the mixture. The lipid film was hydrated in 1 mL of HK buffer (50 mM HEPES, pH 7.4, and 120 mM K-Acetate) to a concentration of 2 mM phospholipid and freeze-thawed five times in liquid nitrogen. Prior to use, 500 µL of liposomes were extruded 19x through a polycarbonate filter of 0.2 µm pore size using a mini-extruder. Extruded liposomes were stored at room temp and used within 2 days following extrusion.

Limited proteolysis

Prior to the experiment, proteins were centrifuged 10 min at 20,000 g, 4°C, to remove any precipitate, and diluted in HK buffer (50 mM HEPES, pH 7.4, and 120 mM K-Acetate) containing 1 mM $MgCl_2$ to 0.1 mg/mL. was mixed or not with diphytanoyl (50% PC, 50% PS) liposomes at 1:1000 protein-to-phospholipid molar ratio in 120 µL final volume. The mix was incubated for 10 min at 25°C with 300 rpm agitation prior to addition of 0.2 µg/mL of subtilisin. At indicated times, 20 µL of the reaction was removed and the reaction was stopped immediately with 2mM PMSF. Samples were analyzed by SDS-PAGE and proteins were stained with Silver stain.

Limited proteolysis of fibrils formed by MBP-PLIN4 constructs (1mg/ml) was carried out using pronase at final concentration of 0.1 mg/ml for 30 minutes at 20°C in the assembly buffer. Pronase digestion was confirmed by SDS-PAGE where the MBP-PLIN4 fusion protein band completely disappear within 30 minutes. At 30 minutes an aliquot was withdrawn immediately to prepare electron microscopy grids for negative stain and cryo-EM, as described.

Artificial LD preparation

Artificial LDs with 13.3 µM DOPC were prepared in 50 mM HEPES, pH 7.4, and 120 mM K-Acetate (HK) buffer and extruded through polycarbonate filters of 8-µm pore size using a mini-extruder (Avanti Polar Lipids), as described [33]. All lipids were from Avanti polar lipids, except TG(18:1/18:1/18:1) and BVO (CAS: 8016-94-2), which were from Sigma and Spectrum Chemical

MFG Corp, respectively. Contaminants such as free FA were removed from BVO as described (Araujo et al. 2024). Purified BVO was dissolved in chloroform and stored at -20°C under argon. To prepare aLDs of defined density, close to the density of the HK buffer, and diameter, we relied on the equations described in [33]. Note that the aLD density was verified experimentally to make sure that the aLDs were efficiently deposited on Ibidi slides for observation by confocal microscopy. For a volume fraction of 0.75% oil in buffer, obtaining a suspension of aLDs with a calculated diameter of 10 µm, adapted for visual analysis by confocal fluorescent microscopy, requires a concentration of phospholipid [PL] = 12.5 µM. To prepare the aLDs, we first mixed 10 µL of triolein (9.11 mg) and 5 µL of BVO (6.6 mg) from stock solutions in chloroform (≈ 90 mg/ml). For 10 µm aLDs, the mix was supplemented with 25 nmol of DOPC (18:1/18:1)) and 0.125 nmol Rhodamine-PE for microscopy experiments. After evaporation of chloroform under a stream of argon (~30 min using a low flow rate), the final oil droplet containing the phospholipids was resuspended in 2 mL HKMD buffer (HEPES 50 mM pH 7.2, K acetate 120 mM, MgCl2 1 mM, DTT 1 mM), hence leading to a 0.75% oil suspension. The suspension was briefly vortexed and pipetted 5x with a Hamilton syringe, then extruded 19 times through 8 µm polycarbonate filters using a hand mini extruder (Avanti). Note that extrusion through this pore size yields aLDs approximatelly 10 µm in diameter when assessed by dynamic light scattering [33]. The aLDs were kept at room temperature under argon, protected from light, and used on the same day.

Analysis of protein binding to artificial LDs

In a clean glass tube, 500 µL final volume of freshly prepared artificial LD suspension was gently mixed with 0.25 µM of protein, where 1/5th is fluorescently labelled with AlexaFluor-488, in a final volume of 600 µl (in HK buffer supplemented with 1mM MgCl2 and 1mM DTT). The binding of proteins to LDs was then immediatelly analyzed by confocal fluorescent microscopy, or following a 24h incubation at at room temp before observation. For microscopy observation, 30 µL of the LD-protein mixture was gently deposited on an 8-well Ibidi slide and containing 80 µL of buffer, incubated for 15 min to allow the LDs to attach to the surface of the slide and observed by a spinning disk microscope.

ThT aggregation assay in the presence of LDs or liposomes

Before experiment, aliquot of unilamellar DOPC liposome suspension (2 mM DOPC) were thawed at room temperature and then extruded through a 0.4 µm diameter filter. For LDs, 13.3 µM DOPC aLDs were freshly prepared and extruded through a 8 µm diameter filter. Different volumes of aLDs (0 µL, 10 µL, 50 µL or 100 µL) or liposomes (0 µL, 10 µL or 100 µL) were added to wells of a Greiner BlackPlate 96 Flat along with different PLIN4 fragments, as indicated: 4mer[260:] (0.125 mg/mL, [mer] = 9.5 µM), 12mer[260:] (1 mg/mL, [mer] = 26 µM) or 12merMUT (0.125mg/mL [mer] = 3.2 µM). The protein concentrations were chosen such as to assure good aggregation kinetics and minimize the total amount of protein required, based on previous experiments in the absence of lipids, and thus differed between different constructs. For each condition, the molar ratio between [PC] and individual 33-aa PLIN4 repeats [mer] was calculated. Note that the PC concentration of liposomes is >100x higher than in the case of LDs, due to the smaller size of liposomes. However, since the liposomes are composed of a bilayer, compared to the LD monolayer, the PC concentration in the case of liposomes should be divided by 2 to obtain the total PC area available for protein binding, compare to LDs, assuming that the liposomes remain

intact during the course of the experiment. This is difficult to verify due to adsorption of liposomes/LDs to the sides of the wells during the course of the experiment.

Confocal microscopy and image analysis

Observations of PLIN4-12mer[260:] and PLIN4-12merMUT aggregates after ThT assay were performed with an Axioimager Z2 Upright Zeiss microscope using 40X EC Plan Neofluar 1.4 NA oil-immersion objective. Images were acquired with scMOS ZYLA 4.2 MP camera and a CFP filter. The system was driven by Metamorph software. Observations of aLDs were performed with an inverted Olympus Ixplore Spin SR microscope coupled with a spinning disk CSU-W1 head (Yokogawa) using 60X UPLXAPO 1.42 NA DT 0.15mm oil-immersion objective. Z stacks of 10 images with a step size of 0.5 µm were acquired with sCMOS Fusion BT Hamamatsu camera, using 488 nm and 561 nm (100 mW) lasers with GFP Narrow filter. The system was driven by CellSens Dimension 3.2 software. Yeast were observed using the same microscopy set-up. Multi-dimensional images of PLIN4-GFP in live HeLa cells were acquired at 37°C with an LSM980-NLO confocal microscope (Zeiss), using a 63X Plan-Apo 1.4NA oil-immersion objective. The microscope is equipped with T-PMT camera and driven by Zeiss Zen Blue software. Excitation sources used were: 405 nm diode laser and an Argon laser for 488 nm. Images were analyzed using Image-J. Aggregates in yeast were quantified manually. Data was plotted using GraphPad.

References

1. Soto, C., and Pritzkow, S. (2018). Protein misfolding, aggregation, and conformational strains in neurodegenerative diseases. Nat. Neurosci. *21*, 1332–1340. https://doi.org/10.1038/s41593-018-0235-9.

2. Iadanza, M.G., Jackson, M.P., Hewitt, E.W., Ranson, N.A., and Radford, S.E. (2018). A new era for understanding amyloid structures and disease. Nat. Rev. Mol. Cell Biol. *19*, 755–773. https://doi.org/10.1038/s41580-018-0060-8.

3. Conway, K.A., Harper, J.D., and Lansbury, P.T. (1998). Accelerated in vitro fibril formation by a mutant α-synuclein linked to early-onset Parkinson disease. Nat. Med. *4*, 1318–1320. https://doi.org/10.1038/3311.

4. Guerrero-Ferreira, R., Taylor, N.M., Mona, D., Ringler, P., Lauer, M.E., Riek, R., Britschgi, M., and Stahlberg, H. (2018). Cryo-EM structure of alpha-synuclein fibrils. eLife *7*, 43. https://doi.org/10.7554/elife.36402.

5. Scheres, S.H., Zhang, W., Falcon, B., and Goedert, M. (2020). ScienceDirect Cryo-EM structures of tau filaments. Curr. Opin. Struct. Biol. *64*, 17–25. https://doi.org/10.1016/j.sbi.2020.05.011.

6. Scheres, S.H.W., Ryskeldi-Falcon, B., and Goedert, M. (2023). Molecular pathology of neurodegenerative diseases by cryo-EM of amyloids. Nature *621*, 701–710. https://doi.org/10.1038/s41586-023-06437-2.

7. Gonay, V., Dunne, M.P., Caceres-Delpiano, J., and Kajava, A.V. (2025). Developing machine-learning-based amyloidogenicity predictors with Cross-Beta DB. Alzheimers Dement. *21*, e14510. https://doi.org/10.1002/alz.14510.

8. Ulamec, S.M., Brockwell, D.J., and Radford, S.E. (2020). Looking Beyond the Core: The Role of Flanking Regions in the Aggregation of Amyloidogenic Peptides and Proteins. Front. Neurosci. *14*, 611285. https://doi.org/10.3389/fnins.2020.611285.

9. Falgarone, T., Villain, E., Richard, F., Osmanli, Z., and Kajava, A.V. (2023). Census of exposed aggregation-prone regions in proteomes. Brief. Bioinform. *24*, bbad183. https://doi.org/10.1093/bib/bbad183.

10. Auluck, P.K., Caraveo, G., and Lindquist, S. (2010). α-Synuclein: Membrane Interactions and Toxicity in Parkinson's Disease. Annu. Rev. Cell Dev. Biol. *26*, 211–233. https://doi.org/10.1146/annurev.cellbio.042308.113313.

11. Rodriguez, J.A., Ivanova, M.I., Sawaya, M.R., Cascio, D., Reyes, F.E., Shi, D., Sangwan, S., Guenther, E.L., Johnson, L.M., Zhang, M., et al. (2015). Structure of the toxic core of α-synuclein from invisible crystals. Nature *525*, 486–490. https://doi.org/10.1038/nature15368.

12. Crowther, R.A., Olesen, O.F., Jakes, R., and Goedert, M. (1992). The microtubule binding repeats of tau protein assemble into filaments like those found in Alzheimer's disease. FEBS Lett. *309*, 199–202. https://doi.org/10.1016/0014-5793(92)81094-3.

13. Buchholz, S., and Zempel, H. (2024). The six brain-specific TAU isoforms and their role in Alzheimer's disease and related neurodegenerative dementia syndromes. Alzheimers Dement. *20*, 3606–3628. https://doi.org/10.1002/alz.13784.

14. Elena-Real, C.A., Sagar, A., Urbanek, A., Popovic, M., Morató, A., Estaña, A., Fournet, A., Doucet, C., Lund, X.L., Shi, Z.-D., et al. (2023). The structure of pathogenic huntingtin exon 1 defines the bases of its aggregation propensity. Nat. Struct. Mol. Biol. *30*, 309–320. https://doi.org/10.1038/s41594-023-00920-0.

15. Scherzinger, E., Lurz, R., Turmaine, M., Mangiarini, L., Hollenbach, B., Hasenbank, R., Bates, G.P., Davies, S.W., Lehrach, H., and Wanker, E.E. (1997). Huntingtin-Encoded Polyglutamine Expansions Form Amyloid-like Protein Aggregates In Vitro and In Vivo. Cell *90*, 549–558. https://doi.org/10.1016/S0092-8674(00)80514-0.

16. Di Blasi, C., Moghadaszadeh, B., Ciano, C., Negri, T., Giavazzi, A., Cornelio, F., Morandi, L., and Mora, M. (2004). Abnormal lysosomal and ubiquitin-proteasome pathways in 19p13.3 distal myopathy. Ann. Neurol. *56*, 133–138. https://doi.org/10.1002/ana.20158.

17. Savarese, M., Sarparanta, J., Vihola, A., Jonson, P.H., Johari, M., Rusanen, S., Hackman, P., and Udd, B. (2020). Panorama of the distal myopathies. Acta Myol. Myopathies Cardiomyopathies Off. J. Mediterr. Soc. Myol. *39*, 245–265. https://doi.org/10.36185/2532-1900-028.

18. Maggi, L., Gibertini, S., Iannibelli, E., Gallone, A., Bonanno, S., Cazzato, D., Gerevini, S., Moscatelli, M., Blasevich, F., Riolo, G., et al. (2023). PLIN4-related myopathy: clinical, histological and imaging data in a large cohort of patients. J. Neurol. *270*, 4538–4543. https://doi.org/10.1007/s00415-023-11729-8.

19. Ruggieri, A., Naumenko, S., Smith, M.A., Iannibelli, E., Blasevich, F., Bragato, C., Gibertini, S., Barton, K., Vorgerd, M., Marcus, K., et al. (2020). Multiomic elucidation of a coding 99-mer repeat-expansion skeletal muscle disease. Acta Neuropathol. (Berl.) *590*, 4171. https://doi.org/10.1007/s00401-020-02164-4.

20. Campisi, D., Hawkins, N., Bonjour, K., and Wollert, T. (2025). The Role of WIPI2, ATG16L1 and ATG12-ATG5 in selective and nonselective autophagy. J. Mol. Biol., 169138. https://doi.org/10.1016/j.jmb.2025.169138.

21. Gibertini, S., Ruggieri, A., Cheli, M., and Maggi, L. (2023). Protein Aggregates and Aggrephagy in Myopathies. Int. J. Mol. Sci. *24*. https://doi.org/10.3390/ijms24098456.

22. Copic, A., Antoine-Bally, S., Giménez-Andŕes, M., Garay, C.L.T., Antonny, B., Manni, M.M., Pagnotta, S., Guihot, J., and Jackson, C.L. (2018). A giant amphipathic helix from a perilipin that is adapted for coating lipid droplets. Nat. Commun. *9*, 1332. https://doi.org/10.1038/s41467-018-03717-8.

23. Bussel, J., and Eliezer, D. (2003). A Structural and Functional Role for 11-mer Repeats in \textbackslashalpha\-Synuclein and Other Exchangeable Lipid Binding Proteins. J. Mol. Biol. *329*, 763–778. https://doi.org/10.1016/s0022-2836(03)00520-5.

24. Wang, Q., Yu, M., Zhang, W., Gang, Q., Xie, Z., Xu, J., Zhou, C., Wang, D., Meng, L., Lv, H., et al. (2022). Subsarcolemmal and cytoplasmic p62 positivity and rimmed vacuoles are distinctive for PLIN4-myopathy. Ann. Clin. Transl. Neurol. https://doi.org/10.1002/acn3.51666.

25. Yang, K., Zeng, Y.-H., Qiu, Y.-S., Lin, F., Chen, H.-Z., Jin, M., Chen, L., Zheng, F.-Z., Ding, Y.-L., Cao, C.-Y., et al. (2022). Expanding the phenotype and genotype spectra of PLIN4-associated myopathy with rimmed ubiquitin-positive autophagic vacuolation. Acta Neuropathol. (Berl.) *143*, 733–735. https://doi.org/10.1007/s00401-022-02422-7.

26. Griseti, E., Bello, A.A., Bieth, E., Sabbagh, B., Iacovoni, J.S., Bigay, J., Laurell, H., and Copic, A. (2023). Molecular mechanisms of perilipin protein function in lipid droplet metabolism. FEBS Lett. https://doi.org/10.1002/1873-3468.14792.

27. Klemm, R.W., and Carvalho, P. (2024). Lipid Droplets Big and Small: Basic Mechanisms That Make Them All. Annu. Rev. Cell Dev. Biol. *40*, 143–168. https://doi.org/10.1146/annurev-cellbio-012624-031419.

28. Bosma, M. (2016). Lipid droplet dynamics in skeletal muscle. Exp. Cell Res. *340*, 180–186. https://doi.org/10.1016/j.yexcr.2015.10.023.

29. Seibert, J.T., Najt, C.P., Heden, T.D., Mashek, D.G., and Chow, L.S. (2020). Muscle Lipid Droplets: Cellular Signaling to Exercise Physiology and Beyond. Trends Endocrinol. Metab. *31*, 928–938. https://doi.org/10.1016/j.tem.2020.08.002.

30. Pourteymour, S., Lee, S., Langleite, T.M., Eckardt, K., Hjorth, M., Bindesbøll, C., Dalen, K.T., Birkeland, K.I., Drevon, C.A., Holen, T., et al. (2015). Perilipin 4 in human skeletal muscle: localization and effect of physical activity. Physiol. Rep. *3*. https://doi.org/10.14814/phy2.12481.

31. Wolins, N.E., Quaynor, B.K., Skinner, J.R., Tzekov, A., Croce, M.A., Gropler, M.C., Varma, V., Yao-Borengasser, A., Rasouli, N., Kern, P.A., et al. (2006). OXPAT/PAT-1 Is a PPAR-Induced Lipid Droplet Protein That Promotes Fatty Acid Utilization. Diabetes *55*, 3418–3428. https://doi.org/10.2337/db06-0399.

32. Wolins, N.E., Quaynor, B.K., Skinner, J.R., Schoenfish, M.J., Tzekov, A., and Bickel, P.E. (2005). S3-12, Adipophilin, and TIP47 package lipid in adipocytes. J. Biol. Chem. *280*, 19146–19155. https://doi.org/10.1074/jbc.m500978200.

33. Araújo, A.R.D., Bello, A.A., Bigay, J., Franckhauser, C., Gautier, R., Cazareth, J., Kovacs, D., Brau, F., Fuggetta, N., Copic, A., et al. (2024). Surface tension-driven sorting of human perilipins on lipid droplets. J Cell Biol *223*. https://doi.org/10.1083/jcb.202403064.

34. Koprulu, M., Zhao, Y., Wheeler, E., Dong, L., Rocha, N., Li, C., Griffin, J.D., Patel, S., Streek, M.V. de, Glastonbury, C.A., et al. (2022). Identification of Rare Loss-of-Function Genetic Variation Regulating

Body Fat Distribution. J. Clin. Endocrinol. Metab. *107*, 1065–1077. https://doi.org/10.1210/clinem/dgab877.

35. Giménez-Andŕes, M., c, T.E. si\textbackslashv, Antoine-Bally, S., D'Ambrosio, J.M., Antonny, B., Derganc, J., and Copic, A. (2021). Exceptional stability of a perilipin on lipid droplets depends on its polar residues, suggesting multimeric assembly. eLife *10*. https://doi.org/10.7554/elife.61401.
36. Cole, N.B., Murphy, D.D., Grider, T., Rueter, S., Brasaemle, D., and Nussbaum, R.L. (2002). Lipid Droplet Binding and Oligomerization Properties of the Parkinson's Disease Protein \textbackslashtextasciitilde-Synuclein. J. Biol. Chem. *277*, 6344–6352. https://doi.org/10.1074/jbc.m108414200.
37. Girard, V., Jollivet, F., Knittelfelder, O., Celle, M., Arsac, J.-N., Chatelain, G., Brink, D.M.V. den, Baron, T., Shevchenko, A., Kühnlein, R.P., et al. (2021). Abnormal accumulation of lipid droplets in neurons induces the conversion of alpha-Synuclein to proteolytic resistant forms in a Drosophila model of Parkinson's disease. PLoS Genet. *17*, e1009921. https://doi.org/10.1371/journal.pgen.1009921.
38. Fanning, S., Selkoe, D., and Dettmer, U. (2020). Parkinson's disease: proteinopathy or lipidopathy? Npj Park. Dis. *6*, 3. https://doi.org/10.1038/s41531-019-0103-7.
39. Roberts, M.A., and Olzmann, J.A. (2020). Protein Quality Control and Lipid Droplet Metabolism. Annu. Rev. Cell Dev. Biol. *36*, 115–139. https://doi.org/10.1146/annurev-cellbio-031320-101827.
40. Shahmoradian, S.H., Lewis, A.J., Genoud, C., Hench, J., Moors, T.E., Navarro, P.P., Castaño-Díez, D., Schweighauser, G., Graff-Meyer, A., Goldie, K.N., et al. (2019). Lewy pathology in Parkinson's disease consists of crowded organelles and lipid membranes. Nat. Neurosci. *22*, 1099–1109. https://doi.org/10.1038/s41593-019-0423-2.
41. Wolins, N.E., Skinner, J.R., Schoenfish, M.J., Tzekov, A., Bensch, K.G., and Bickel, P.E. (2003). Adipocyte protein S3-12 coats nascent lipid droplets. J. Biol. Chem. *278*, 37713–37721. https://doi.org/10.1074/jbc.m304025200.
42. Xue, C., Lin, T.Y., Chang, D., and Guo, Z. (2017). Thioflavin T as an amyloid dye: fibril quantification, optimal concentration and effect on aggregation. R. Soc. Open Sci. *4*, 160696–12. https://doi.org/10.1098/rsos.160696.
43. Reynaud, A., Magdeleine, M., Patel, A., Gay, A.-S., Debayle, D., Abelanet, S., and Antonny, B. (2022). Tumor protein D54 binds intracellular nanovesicles via an extended amphipathic region. J. Biol. Chem. *298*, 102136. https://doi.org/10.1016/j.jbc.2022.102136.
44. Aubrey, L.D., Blakeman, B.J.F., Lutter, L., Serpell, C.J., Tuite, M.F., Serpell, L.C., and Xue, W.-F. (2020). Quantification of amyloid fibril polymorphism by nano-morphometry reveals the individuality of filament assembly. Commun. Chem. *3*, 125. https://doi.org/10.1038/s42004-020-00372-3.
45. Ahmed, A.B., Znassi, N., Chˆateau, M.-T., and Kajava, A.V. (2015). A structure-based approach to predict predisposition to amyloidosis. Alzheimers Dement. J. Alzheimers Assoc. *11*, 681–690. https://doi.org/10.1016/j.jalz.2014.06.007.
46. Falgarone, T., Villain, É., Guettaf, A., Leclercq, J., and Kajava, A.V. (2022). TAPASS: Tool for annotation of protein amyloidogenicity in the context of other structural states. J. Struct. Biol. *214*, 107840. https://doi.org/10.1016/j.jsb.2022.107840.
47. Fernandez-Escamilla, A.-M., Rousseau, F., Schymkowitz, J., and Serrano, L. (2004). Prediction of sequence-dependent and mutational effects on the aggregation of peptides and proteins. Nat. Biotechnol. *22*, 1302–1306. https://doi.org/10.1038/nbt1012.

48. Walsh, I., Seno, F., Tosatto, S.C.E., and Trovato, A. (2014). PASTA 2.0: an improved server for protein aggregation prediction. Nucleic Acids Res. *42*, W301–W307. https://doi.org/10.1093/nar/gku399.

49. Bartz, R., Li, W.-H., Venables, B., Zehmer, J.K., Roth, M.R., Welti, R., Anderson, R.G.W., Liu, P., and Chapman, K.D. (2007). Lipidomics reveals that adiposomes store ether lipids and mediate phospholipid traffic. J. Lipid Res. *48*, 837–847. https://doi.org/10.1194/jlr.m600413-jlr200.

50. Jacquier, N., Mishra, S., Choudhary, V., and Schneiter, R. (2013). Expression of oleosin and perilipins in yeast promotes formation of lipid droplets from the endoplasmic reticulum. J. Cell Sci. *126*, 5198–5209. https://doi.org/10.1242/jcs.131896.

51. Rowe, E.R., Mimmack, M.L., Barbosa, A.D., Haider, A., Isaac, I., Ouberai, M.M., Thiam, A.R., Patel, S., Saudek, V., Siniossoglou, S., et al. (2016). Conserved Amphipathic Helices Mediate Lipid Droplet Targeting of Perilipins 1–3. J. Biol. Chem. *291*, 6664–6678. https://doi.org/10.1074/jbc.m115.691048.

52. Escusa-Toret, S., Vonk, W.I.M., and Frydman, J. (2013). Spatial sequestration of misfolded proteins by a dynamic chaperone pathway enhances cellular fitness during stress. Nat. Cell Biol. *15*, 1231–1243. https://doi.org/10.1038/ncb2838.

53. Fanning, S., Haque, A., Imberdis, T., Baru, V., Barrasa, M.I., Nuber, S., Termine, D., Ramalingam, N., Ho, G.P.H., Noble, T., et al. (2019). Lipidomic Analysis of \textbackslashalpha\-Synuclein Neurotoxicity Identifies Stearoyl CoA Desaturase as a Target for Parkinson Treatment. Mol. Cell *73*, 1001-1014.e8. https://doi.org/10.1016/j.molcel.2018.11.028.

54. Outeiro, T.F., and Lindquist, S. (2003). Yeast cells provide insight into alpha-synuclein biology and pathobiology. Science *302*, 1772–1775. https://doi.org/10.1126/science.1090439.

55. Tardiff, D.F., Khurana, V., Chung, C.Y., and Lindquist, S. (2014). From yeast to patient neurons and back again: Powerful new discovery platforms. Mov. Disord. *29*, 1231–1240. https://doi.org/10.1002/mds.25989.

56. Mumberg, D., Müller, R., and Funk, M. (1995). Yeast vectors for the controlled expression of heterologous proteins in different genetic backgrounds. Gene *156*, 119–122.

57. Bösl, B., Grimminger, V., and Walter, S. (2006). The molecular chaperone Hsp104—A molecular machine for protein disaggregation. J. Struct. Biol. *156*, 139–148. https://doi.org/10.1016/j.jsb.2006.02.004.

58. Peelaerts, W., Bousset, L., Perren, A.V. der, Moskalyuk, A., Pulizzi, R., Giugliano, M., Haute, C.V. den, Melki, R., and Baekelandt, V. (2015). \textbackslashalpha\-Synuclein strains cause distinct synucleinopathies after local and systemic administration. Nature *522*, 340–344. https://doi.org/10.1038/nature14547.

59. Kedia, N., Arhzaouy, K., Pittman, S.K., Sun, Y., Batchelor, M., Weihl, C.C., and Bieschke, J. (2019). Desmin forms toxic, seeding-competent amyloid aggregates that persist in muscle fibers. Proc. Natl. Acad. Sci. U. S. A. *116*, 16835–16840. https://doi.org/10.1073/pnas.1908263116.

60. Daskalov, A., Dyrka, W., and Saupe, S.J. (2015). Theme and variations: evolutionary diversification of the HET-s functional amyloid motif. Sci. Rep. *5*, 12494. https://doi.org/10.1038/srep12494.

61. Wasmer, C., Lange, A., Melckebeke, H.V., Siemer, A.B., Riek, R., and Meier, B.H. (2008). Amyloid fibrils of the HET-s(218-289) prion form a beta solenoid with a triangular hydrophobic core. Science *319*, 1523–1526. https://doi.org/10.1126/science.1151839.

62. Chapman, M.R., Robinson, L.S., Pinkner, J.S., Roth, R., Heuser, J., Hammar, M., Normark, S., and Hultgren, S.J. (2002). Role of *Escherichia coli* Curli Operons in Directing Amyloid Fiber Formation. Science *295*, 851–855. https://doi.org/10.1126/science.1067484.

63. Rasmussen, C.B., Christiansen, G., Vad, B.S., Lynggaard, C., Enghild, J.J., Andreasen, M., and Otzen, D. (2019). Imperfect repeats in the functional amyloid protein FapC reduce the tendency to fragment during fibrillation. Protein Sci. *28*, 633–642. https://doi.org/10.1002/pro.3566.

64. Sleutel, M., Pradhan, B., Volkov, A.N., and Remaut, H. (2023). Structural analysis and architectural principles of the bacterial amyloid curli. Nat. Commun. *14*, 2822. https://doi.org/10.1038/s41467-023-38204-2.

65. Sønderby, T.V., Louros, N.N., Khodaparast, L., Khodaparast, L., Madsen, D.J., Olsen, W.P., Moonen, N., Nagaraj, M., Sereikaite, V., Strømgaard, K., et al. (2023). Sequence-targeted Peptides Divert Functional Bacterial Amyloid Towards Destabilized Aggregates and Reduce Biofilm Formation. J. Mol. Biol. *435*, 168039. https://doi.org/10.1016/j.jmb.2023.168039.

66. Wang, X., Zhou, Y., Ren, J.-J., Hammer, N.D., and Chapman, M.R. (2010). Gatekeeper residues in the major curlin subunit modulate bacterial amyloid fiber biogenesis. Proc. Natl. Acad. Sci. *107*, 163–168. https://doi.org/10.1073/pnas.0908714107.

67. Ramazzotti, M., Monsellier, E., Kamoun, C., Degl'Innocenti, D., and Melki, R. (2012). Polyglutamine Repeats Are Associated to Specific Sequence Biases That Are Conserved among Eukaryotes. PLoS ONE *7*, e30824. https://doi.org/10.1371/journal.pone.0030824.

68. Sahtoe, D.D., Andrzejewska, E.A., Han, H.L., Rennella, E., Schneider, M.M., Meisl, G., Ahlrichs, M., Decarreau, J., Nguyen, H., Kang, A., et al. (2024). Design of amyloidogenic peptide traps. Nat. Chem. Biol. *20*, 981–990. https://doi.org/10.1038/s41589-024-01578-5.

69. Alecu, I., and Bennett, S.A.L. (2019). Dysregulated Lipid Metabolism and Its Role in \textbackslashalpha\-Synucleinopathy in Parkinson's Disease. Front. Neurosci. *13*, 328. https://doi.org/10.3389/fnins.2019.00328.

70. Skowronska-Krawczyk, D., and Budin, I. (2020). Aging membranes: Unexplored functions for lipids in the lifespan of the central nervous system. Exp. Gerontol. *131*, 110817. https://doi.org/10.1016/j.exger.2019.110817.

71. Frieg, B., Antonschmidt, L., Dienemann, C., Geraets, J.A., Najbauer, E.E., Matthes, D., Groot, B.L.D., Andreas, L.B., Becker, S., Griesinger, C., et al. (2022). The 3D structure of lipidic fibrils of \textbackslashalpha\-synuclein. Nat. Commun. *13*, 6810–10. https://doi.org/10.1038/s41467-022-34552-7.

72. Habchi, J., Chia, S., Galvagnion, C., Michaels, T.C.T., Bellaiche, M.M.J., Ruggeri, F.S., Sanguanini, M., Idini, I., Kumita, J.R., Sparr, E., et al. (2018). Cholesterol catalyses A\textbackslashbeta\42 aggregation through a heterogeneous nucleation pathway in the presence of lipid membranes. Nat. Chem. *10*, 673–683. https://doi.org/10.1038/s41557-018-0031-x.

73. Vincent, B.M., Tardiff, D.F., Piotrowski, J.S., Aron, R., Lucas, M.C., Chung, C.Y., Bacherman, H., Chen, Y., Pires, M., Subramaniam, R., et al. (2018). Inhibiting Stearoyl-CoA Desaturase Ameliorates α-Synuclein Cytotoxicity. Cell Rep. *25*, 2742-2754.e31. https://doi.org/10.1016/j.celrep.2018.11.028.

74. Frieg, B., Han, M., Giller, K., Dienemann, C., Riedel, D., Becker, S., Andreas, L.B., Griesinger, C., and Schröder, G.F. (2024). Cryo-EM structures of lipidic fibrils of amyloid-\textbackslashbeta\ (1-40). Nat. Commun. *15*, 1297–11. https://doi.org/10.1038/s41467-023-43822-x.

75. Abbott, S.K., Else, P.L., Atkins, T.A., and Hulbert, A.J. (2012). Fatty acid composition of membrane bilayers: Importance of diet polyunsaturated fat balance. BBA - Biomembr. *1818*, 1309–1317. https://doi.org/10.1016/j.bbamem.2012.01.011.

76. Harayama, T., Eto, M., Shindou, H., Kita, Y., Otsubo, E., Hishikawa, D., Ishii, S., Sakimura, K., Mishina, M., and Shimizu, T. (2014). Lysophospholipid Acyltransferases Mediate Phosphatidylcholine Diversification to Achieve the Physical Properties Required In Vivo. Cell Metab. *20*, 295–305. https://doi.org/10.1016/j.cmet.2014.05.019.

77. Olivé, M., Stevanovski, I., Quereda, L.G., Morris, G., Segarra-Casas, A., Rodriguez-Santiago, B., Gallano, P., Alvarez, R., Vesperinas, A., Millan, B.S., et al. (2022). P.156 Novel repeat expansions in PLIN4 in two Spanish families suffering from autosomal dominant distal myopathy with unique pathological features. Neuromuscul. Disord. *32*, S110. https://doi.org/10.1016/j.nmd.2022.07.284.

78. Crooks, G.E., Hon, G., Chandonia, J.-M., and Brenner, S.E. (2004). WebLogo: a sequence logo generator. Genome Res. *14*, 1188–1190. https://doi.org/10.1101/gr.849004.

79. Zimmermann, L., Stephens, A., Nam, S.-Z., Rau, D., Kübler, J., Lozajic, M., Gabler, F., Söding, J., Lupas, A.N., and Alva, V. (2018). A Completely Reimplemented MPI Bioinformatics Toolkit with a New HHpred Server at its Core. J. Mol. Biol. *430*, 2237–2243. https://doi.org/10.1016/j.jmb.2017.12.007.

80. Janke, C., Magiera, M.M., Rathfelder, N., Taxis, C., Reber, S., Maekawa, H., Moreno-Borchart, A., Doenges, G., Schwob, E., Schiebel, E., et al. (2004). A versatile toolbox for PCR-based tagging of yeast genes: new fluorescent proteins, more markers and promoter substitution cassettes. Yeast Chichester Engl. *21*, 947–962. https://doi.org/10.1002/yea.1142.

81. Kowarz, E., Löscher, D., and Marschalek, R. (2015). Optimized Sleeping Beauty transposons rapidly generate stable transgenic cell lines. Biotechnol. J. *10*, 647–653. https://doi.org/10.1002/biot.201400821.

82. Mátés, L., Chuah, M.K.L., Belay, E., Jerchow, B., Manoj, N., Acosta-Sanchez, A., Grzela, D.P., Schmitt, A., Becker, K., Matrai, J., et al. (2009). Molecular evolution of a novel hyperactive Sleeping Beauty transposase enables robust stable gene transfer in vertebrates. Nat. Genet. *41*, 753–761. https://doi.org/10.1038/ng.343.

83. Bousset, L., Pieri, L., Ruiz-Arlandis, G., Gath, J., Jensen, P.H., Habenstein, B., Madiona, K., Olieric, V., Böckmann, A., Meier, B.H., et al. (2013). Structural and functional characterization of two alpha-synuclein strains. Nat. Commun. *4*, 2575. https://doi.org/10.1038/ncomms3575.

84. Scheres, and Sjors, H.W. (2020). Amyloid structure determination in RELION-3.1. Acta Crystallogr. Sect. Struct. Biol. *76*, 94–101. https://doi.org/10.1107/s2059798319016577.

Figure 1

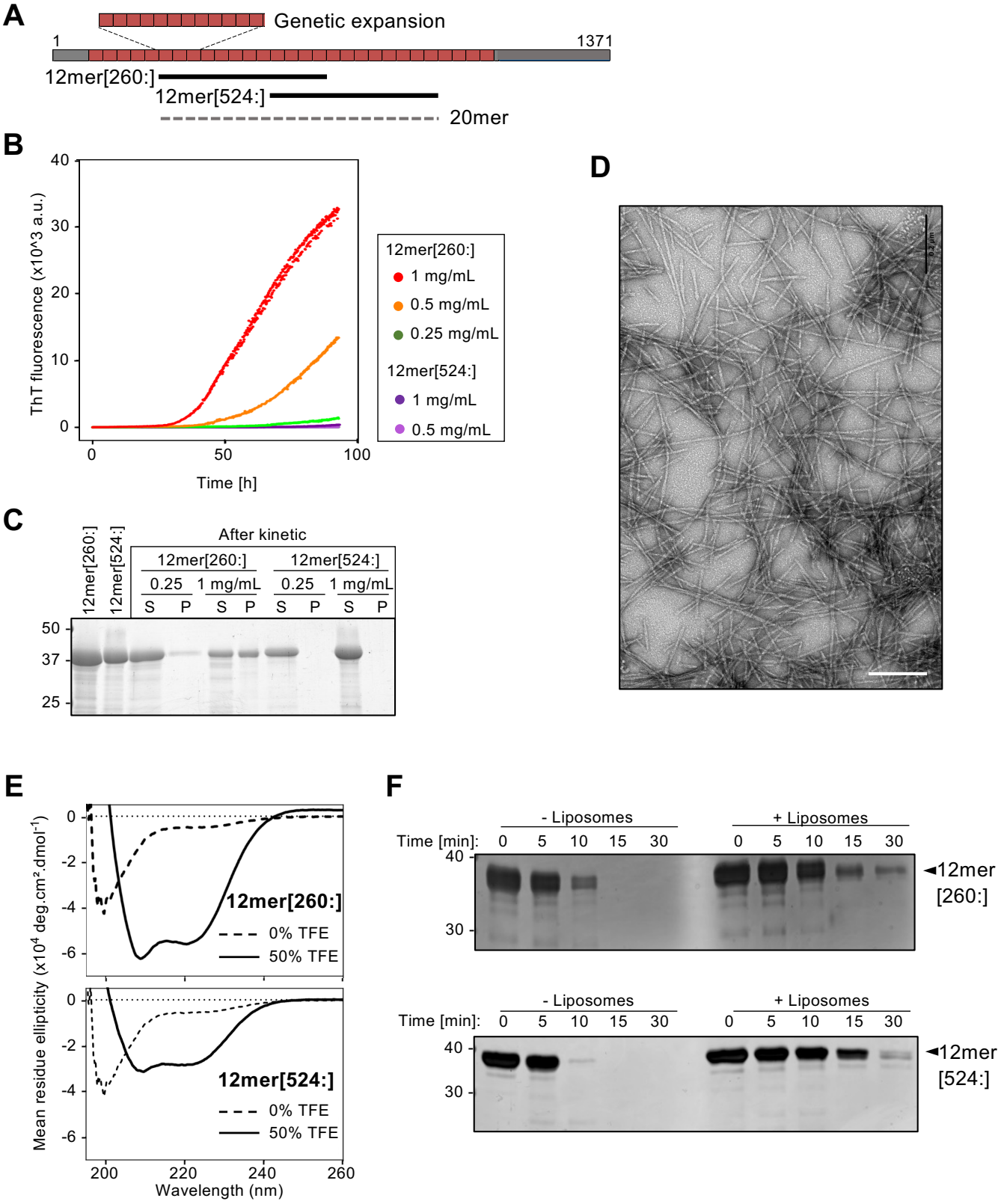
A
Genetic expansion
1
1371
12mer[260:]
12mer[524:]
20mer
B
ThT fluorescence (x10^3 a.u.)
Time [h]
12mer[260:]
1 mg/mL
0.5 mg/mL
0.25 mg/mL
12mer[524:]
1 mg/mL
0.5 mg/mL
C
After kinetic
12mer[260:]
12mer[524:]
0.25
1 mg/mL
S
P
50
37
25
D
E
Mean residue ellipticity (x10^4 deg.cm².dmol^-1)
Wavelength (nm)
12mer[260:]
0% TFE
50% TFE
12mer[524:]
0% TFE
50% TFE
F
- Liposomes
+ Liposomes
Time [min]:
0
5
10
15
30
12mer [260:]
12mer [524:]

Figure 2

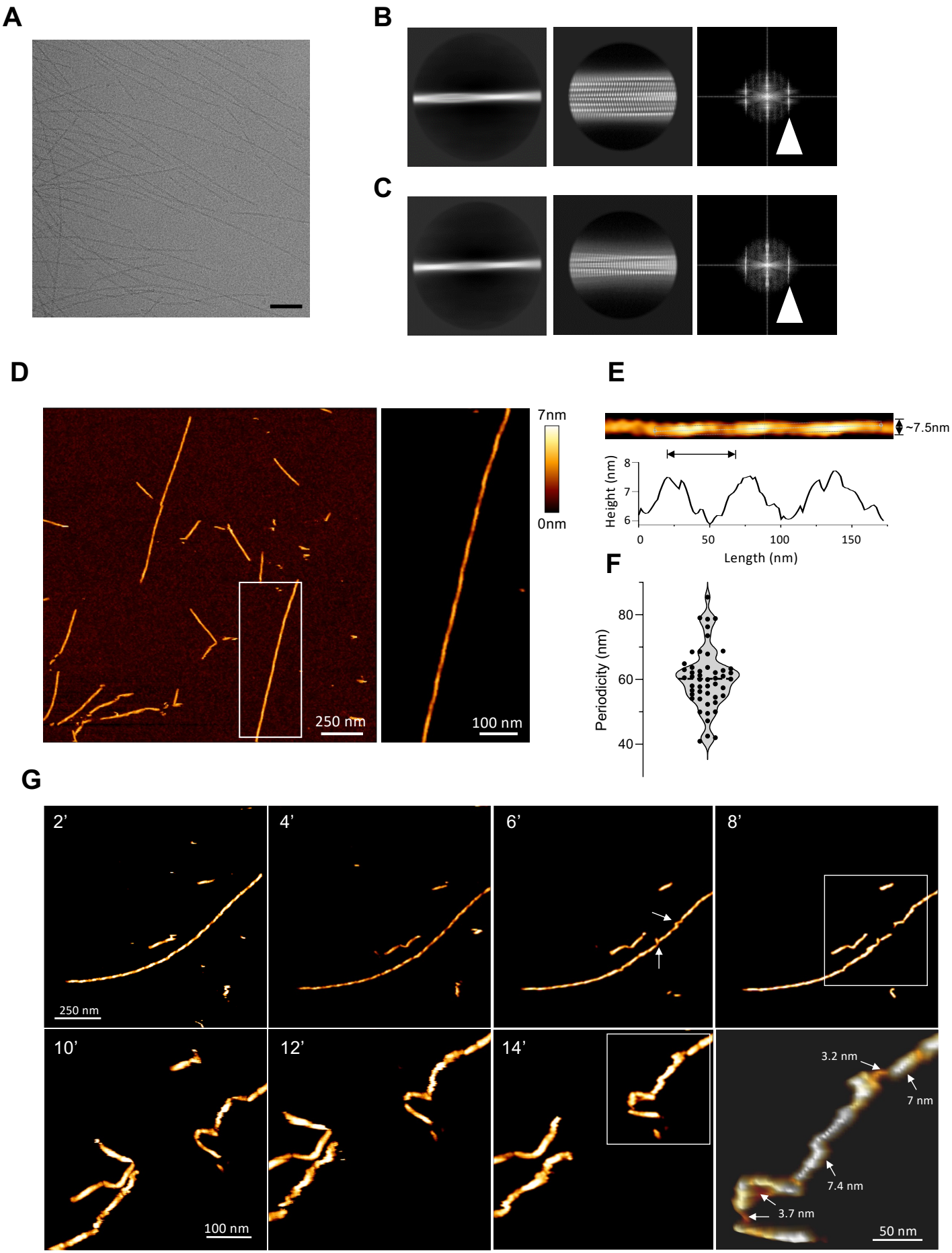
A
B
C
D
7nm
0nm
250 nm
100 nm
E
~7.5nm
Height (nm)
8
7
6
0
50
100
150
Length (nm)
F
Periodicity (nm)
80
60
40
G
2'
4'
6'
8'
250 nm
10'
12'
14'
100 nm
3.2 nm
7 nm
7.4 nm
3.7 nm
50 nm

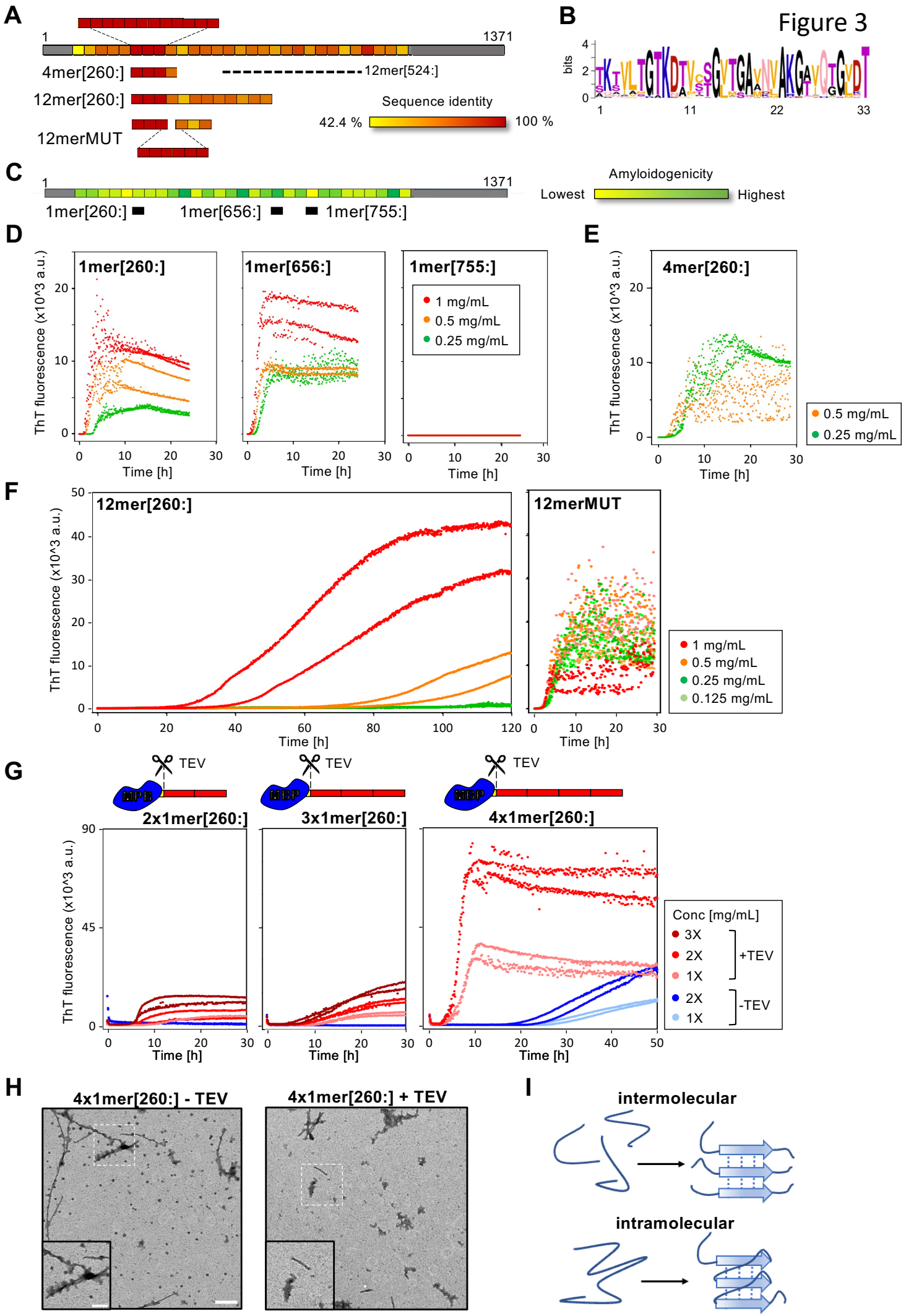
Figure 3
A
1
1371
4mer[260:]
12mer[524:]
12mer[260:]
12merMUT
Sequence identity
42.4 %
100 %
B
bits
1
11
22
33
C
1
1371
1mer[260:]
1mer[656:]
1mer[755:]
Amyloidogenicity
Lowest
Highest
D
1mer[260:]
1mer[656:]
1mer[755:]
1 mg/mL
0.5 mg/mL
0.25 mg/mL
ThT fluorescence (x10^3 a.u.)
Time [h]
E
4mer[260:]
0.5 mg/mL
0.25 mg/mL
F
12mer[260:]
12merMUT
1 mg/mL
0.5 mg/mL
0.25 mg/mL
0.125 mg/mL
G
TEV
MPB
MBP
2x1mer[260:]
3x1mer[260:]
4x1mer[260:]
Conc [mg/mL]
3X
2X
1X
+TEV
2X
1X
-TEV
H
4x1mer[260:] - TEV
4x1mer[260:] + TEV
I
intermolecular
intramolecular

Figure 4

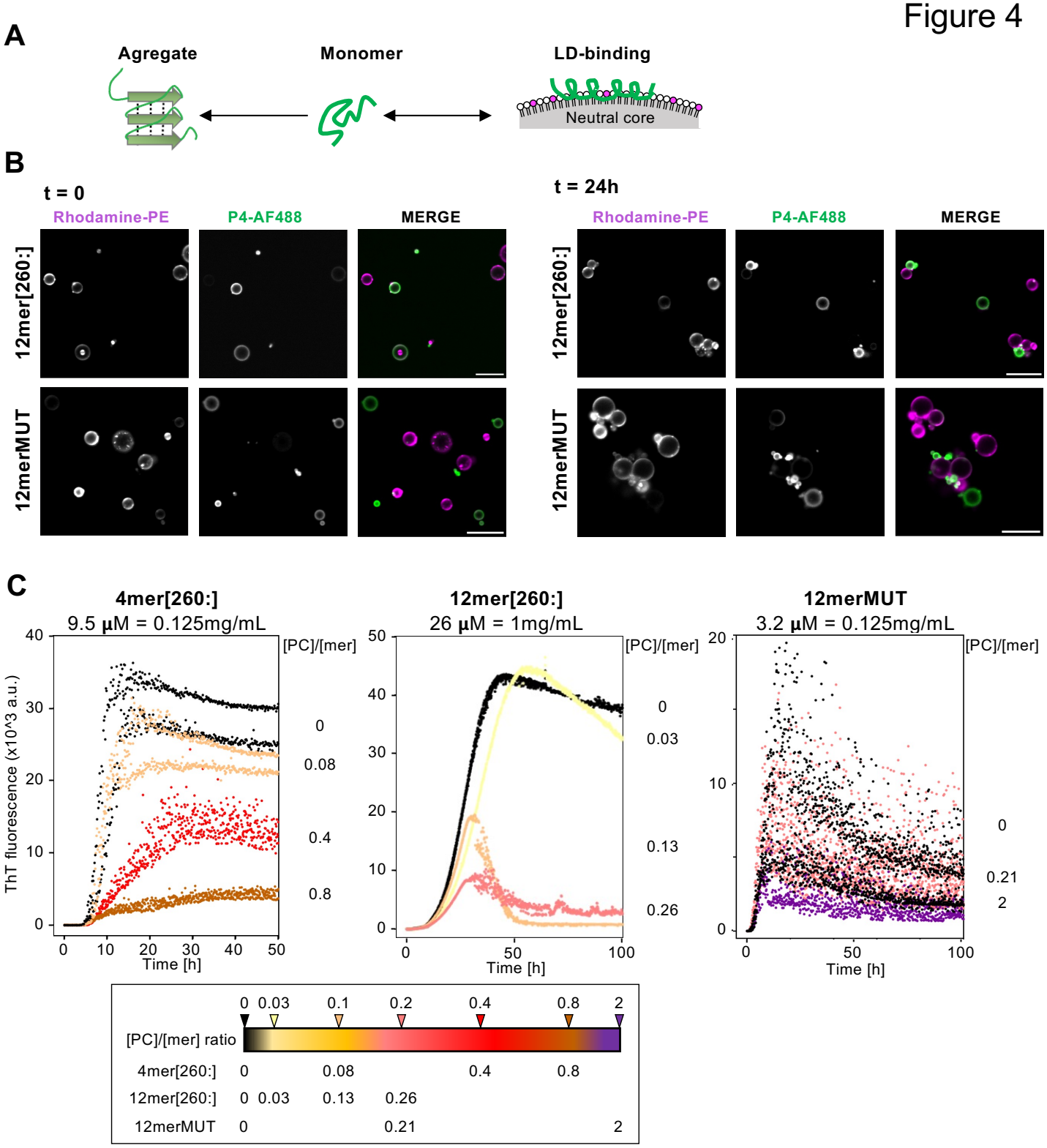
A
Agregate
Monomer
LD-binding
Neutral core
B
t = 0
t = 24h
Rhodamine-PE
P4-AF488
MERGE
12mer[260:]
12merMUT
C
4mer[260:]
9.5 µM = 0.125mg/mL
12mer[260:]
26 µM = 1mg/mL
12merMUT
3.2 µM = 0.125mg/mL
ThT fluorescence (x10^3 a.u.)
Time [h]
[PC]/[mer]
0
0.08
0.4
0.8
0.03
0.13
0.26
0.21
2
[PC]/[mer] ratio
0 0.03 0.1 0.2 0.4 0.8 2
4mer[260:] 0 0.08 0.4 0.8
12mer[260:] 0 0.03 0.13 0.26
12merMUT 0 0.21 2

Figure 5

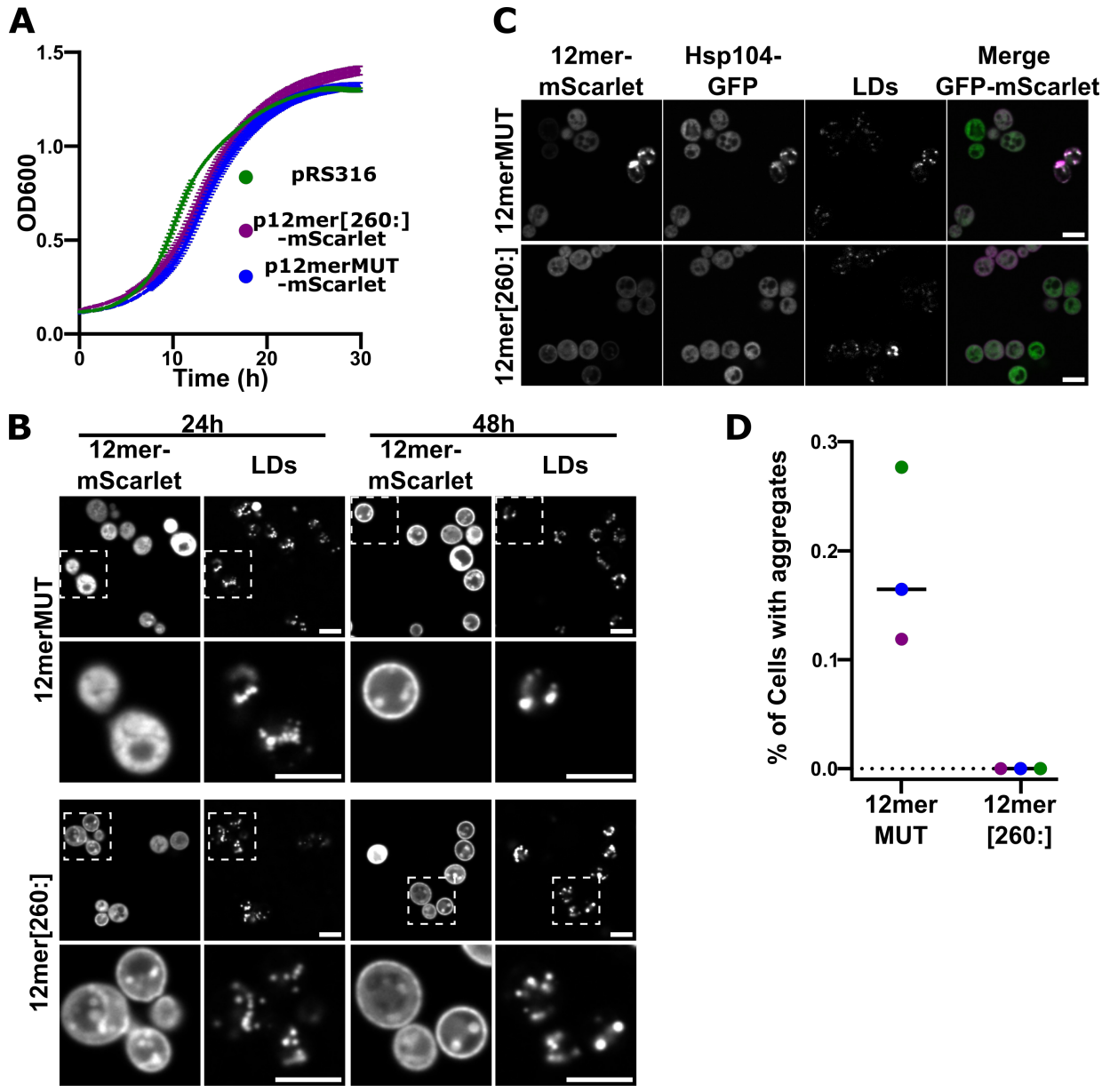
A
OD600
1.5
1.0
0.5
0.0
0
10
20
30
Time (h)
pRS316
p12mer[260:]
-mScarlet
p12merMUT
-mScarlet
C
12mer-
mScarlet
Hsp104-
GFP
LDs
Merge
GFP-mScarlet
12merMUT
12mer[260:]
B
24h
48h
12mer-
mScarlet
LDs
12mer-
mScarlet
LDs
12merMUT
12mer[260:]
D
% of Cells with aggregates
0.3
0.2
0.1
0.0
12mer
MUT
12mer
[260:]